Preprint typeset using LaTeX style emulateapj v. 12/16/11

THE RELATION BETWEEN GALAXY ISM AND CIRCUMGALACTIC O VI GAS KINEMATICS DERIVED FROM OBSERVATIONS AND ΛCDM SIMULATIONS

GLENN G. KACPRZAK[1], JACOB R. VANDER VLIET[3,1], NIKOLE M. NIELSEN[1], SOWGAT MUZAHID[2], STEPHANIE K. POINTON[1], CHRISTOPHER W. CHURCHILL[3], DANIEL CEVERINO[4], KENZ S. ARRAKI[3], ANATOLY KLYPIN[3], JANE C. CHARLTON[5], JAMES LEWIS[3,1]

ABSTRACT

We present the first galaxy–O VI absorption kinematic study for 20 absorption systems (EW>0.1 Å) associated with isolated galaxies ($0.15 \leq z \leq 0.55$) that have accurate redshifts and rotation curves obtained using Keck/ESI. Our sample is split into two azimuthal angle bins: major axis ($\Phi < 25°$) and minor axis ($\Phi > 33°$). O VI absorption along the galaxy major axis is not correlated with galaxy rotation kinematics, with only 1/10 systems that could be explained with rotation/accretion models. This is in contrast to co-rotation commonly observed for Mg II absorption. O VI along the minor axis could be modeled by accelerating outflows but only for small opening angles, while the majority of the O VI is decelerating. Along both axes, stacked O VI profiles reside at the galaxy systemic velocity with the absorption kinematics spanning the entire dynamical range of their galaxies. The O VI found in AMR cosmological simulations exists within filaments and in halos of ∼50 kpc surrounding galaxies. Simulations show that major axis O VI gas inflows along filaments and decelerates as it approaches the galaxy while increasing in its level of co-rotation. Minor axis outflows in the simulations are effective within 50-75 kpc beyond that they decelerate and fall back onto the galaxy. Although the simulations show clear O VI kinematic signatures they are not directly comparable to observations. When we compare kinematic signatures integrated through the entire simulated galaxy halo we find that these signatures are washed out due to full velocity distribution of O VI throughout the halo. We conclude that O VI alone does not serve as a useful kinematic indicator of gas accretion, outflows or star-formation and likely best probes the halo virial temperature.

Subject headings: galaxies: halos — quasars: absorption lines

1. INTRODUCTION

The circumgalactic medium is a massive reservoir of multi-phased gas extending out to 200 kpc and reflects the ongoing physical processes of galaxy evolution. The CGM makes up as much as 50% of baryons around galaxies (Tumlinson et al. 2011; Werk et al. 2014) and the amount of O VI within the CGM is significant (Stocke et al. 2006; Tumlinson et al. 2011; Fox et al. 2013; Stocke et al. 2013; Peeples et al. 2014; Werk et al. 2014) with the vast majority of it bound to the galaxy's gravitational potential (Tumlinson et al. 2011; Stocke et al. 2013; Mathes et al. 2014). However, we are yet to understand the origins and sources of O VI absorption.

It is well known that the O VI equivalent width is anti-correlated with the projected separation from the host galaxy (e.g., Tripp et al. 2008; Wakker & Savage 2009; Chen & Mulchaey 2009; Prochaska et al. 2011; Tumlinson et al. 2011; Mathes et al. 2014; Johnson et al. 2015; Kacprzak et al. 2015). This is similar to the anti-correlation observed between Mg II equivalent width and impact parameter (e.g., Bergeron & Boissé 1991; Steidel 1995; Bouché et al. 2006; Kacprzak et al. 2008; Chen et al. 2010a; Bordoloi et al. 2011; Nielsen et al. 2013b; Kacprzak et al. 2013; Lan et al. 2014; Lan & Mo 2018; Lopez et al. 2018; Rubin et al. 2018). Both O VI and Mg II exhibits a bi-modal azimuthal angle distribution, suggesting a co-spatial behavior and possibly a kinematic connection or origin (Bouché et al. 2012; Kacprzak et al. 2012a, 2015).

It is clear now that the galaxy–Mg II absorption relationship shows strong kinematic preferences consistent with large-scale outflows (Bouché et al. 2006; Tremonti et al. 2007; Martin & Bouché 2009; Weiner et al. 2009; Chelouche & Bowen 2010; Nestor et al. 2011; Noterdaeme et al. 2010; Coil et al. 2011; Kacprzak et al. 2010; Kacprzak et al. 2014; Rubin et al. 2010; Ménard & Fukugita 2012; Martin et al. 2012; Noterdaeme et al. 2012; Krogager et al. 2013; Péroux et al. 2013; Rubin et al. 2014; Crighton et al. 2015; Nielsen et al. 2015, 2016) and co-rotation/accretion (see Kacprzak 2017, for review). Kinematically however, we do not know how O VI relates to its host galaxy.

It is clear that the kinematics of the Mg II and O VI absorption profiles can be very different in shape and velocity spread or they can sometimes be similar (e.g., Werk et al. 2016; Nielsen et al. 2017). Examination of the absorption line profile kinematics and column density ratios has shown that low, intermediate, and high ions may all have a photoionized origin (Tripp et al. 2008; Muzahid et al. 2015; Pachat et al. 2016), while sometimes O VI is commonly found to have a collisionally ionized origin (Tumlinson et al. 2005; Fox et al. 2009; Savage et al. 2011; Tripp et al. 2011; Kacprzak et al. 2012b; Narayanan et al. 2012; Wakker et al. 2012; Meiring et al. 2013; Narayanan et al. 2018; Rosenwasser et al. 2018). This implies that O VI can trace warm/hot coronal regions surrounding galaxies, which may dictate the formation and destruction of the cool/warm CGM (Mo & Miralda-Escude 1996; Maller & Bullock 2004; Dekel & Birnboim 2006) or trace other multi-phase gas structures. Simulations further predict that the O VI may be directly sensitive to the galaxy halo virial temperatures, where O VI peaks for L* galaxies

[1] Swinburne University of Technology, Victoria 3122, Australia gkacprzak@swin.edu.au
[2] Leiden Observatory, Leiden University, P.O. Box 9513, 2300 RA Leiden, The Netherlands
[3] New Mexico State University, Las Cruces, NM 88003, USA
[4] Institut für Theoretische Astrophysik, Zentrum für Astronomie, Universität Heidelberg, Albert-Ueberle-Str. 2, D-69120 Heidelberg, Germany
[5] The Pennsylvania State University, State College, PA 16801, USA

(Oppenheimer et al. 2016) or due to black hole feedback impacting the physical state of the circumgalactic medium (Nelson et al. 2018; Oppenheimer et al. 2018). In addition, Roca-Fàbrega et al. (2018) showed that O VI not only depends on mass but on redshift as well. Photoionization of cold-warm gas dominates during the peak of the meta-galactic UV background ($z = 2$). In massive halos, collisional ionization by thermal electrons become important at $z < 0.5$.

Thus, although Mg II and O VI exhibit some similarities, their differences make it completely unclear as to whether Mg II and O VI are even trace the same kinematic structures.

We aim to further explore the multi-phase azimuthal distribution of O VI absorption to determine whether the relative galaxy-O VI kinematics shows signatures of inflow and outflow along the major and minor axes, respectively. We have acquired Keck/ESI spectra for 20 galaxies to obtain their rotation curves, which will then be compared to the *HST*/COS O VI absorption kinematics. In Section 2 we present our sample, data and data reduction. In Section 3 we present our observational results and simple models for O VI residing along the major and minor axes of galaxies. We provide our interpretation of the data using cosmological simulations in Section 4. In Section 5, we discuss what can be inferred from the results and concluding remarks are offered in Section 6. Throughout we adopt an $H_0 = 70$ km s^{-1}Mpc^{-1}, $\Omega_M = 0.3$, $\Omega_\Lambda = 0.7$ cosmology.

2. GALAXY SAMPLE AND DATA ANALYSIS

We have obtained rotation curves using Keck/ESI for a sample of 20 O VI absorbing galaxies with redshifts ranging between $0.15<z<0.55$ within ~ 300 kpc ($31<D<276$ kpc) of bright background quasars. These galaxies are selected to be isolated such that there are no neighbors within 100 kpc and have velocity separations less than 500 km s^{-1}. These *HST* imaged galaxy–absorber pairs were identified as part of our "Multiphase Galaxy Halos" Survey (from PID 13398 plus from the literature). We discuss the data and analysis below.

2.1. *Quasar Spectroscopy*

The *HST*/COS quasar spectra have a resolution of $R \sim$20,000 and covers the O VI $\lambda\lambda$1031, 1037 doublet for the targeted galaxies. Details of the *HST*/COS observations are presented in Kacprzak et al. (2015). The data were reduced using the CALCOS software. Individual grating integrations were aligned and co-added using the IDL code 'coadd_x1d' developed by Danforth et al. (2010)[6]. Since the COS FUV spectra are over-sampled (six pixels per resolution element) we binned the data by three pixels to increase the signal-to-noise ratio and all of our analysis was performed on the binned spectra. Continuum normalization was performed by fitting the absorption-free regions with smooth low-order polynomials.

We adopted the fitted rest-frame equivalent widths (EWs) and column densities from Kacprzak et al. (2015). Non-Gaussian line spread functions (LSF) were adopted and were obtained by interpolating the LSF tables (Kriss 2011) at the observed central wavelength for each absorption line and was convolved with the fitted model Voigt profile VPFIT (Carswell & Webb 2014). In all cases, a minimum number of components was used to obtain a satisfactory fit with reduced $\chi^2 \sim 1$. The O VI λ 1031 model profiles were used to compute the EWs and the 1σ errors were computed using the error spectrum. Both the EWs and column densities are listed in Table 1.

[6] http://casa.colorado.edu/danforth/science/cos/costools.html

2.2. *HST Imaging and Galaxy Models*

All quasar/galaxy fields have been imaged with *HST* using either ACS, WFC3 or WFPC2. Details of the observations are found in Kacprzak et al. (2015) and the filters used are found in Table 1. ACS and WFC3 data were reduced using the DrizzlePac software (Gonzaga et al. 2012). When enough frames were present, cosmic rays were removed during the multidrizzle process otherwise, L.A.Cosmic was used (van Dokkum 2001). WFPC–2 data were reduced using the WFPC2 Associations Science Products Pipeline (WASPP) (see Kacprzak et al. 2011b).

Galaxy photometry was adopted from Kacprzak et al. (2015), who used the Source Extractor software (SExtractor; Bertin & Arnouts 1996) with a detection criterion of 1.5 σ above background. The m_{HST} magnitudes in each filter are quoted in the AB system and are listed in Table 1.

We adopt calculated halo masses and virial radii from Ng et al. (2019), who applied halo abundance matching methods in the Bolshoi N-body cosmological simulation (Klypin et al. 2011); see Churchill et al. (2013a,b) for further details.

The galaxy morphological parameters and orientations are adopted from Kacprzak et al. (2015). In summary, morphological parameters were quantified by fitting a two-component disk+bulge model using GIM2D (Simard et al. 2002), where the disk component has an exponential profile while the bulge has a Sérsic profile (Sérsic 1968) with $0.2 \leq n \leq 4.0$. The galaxy properties are listed in Table 1. We use the standard convention of the azimuthal angle $\Phi = 0°$ to be along the galaxy projected major axis and $\Phi = 90°$ to be along the galaxy projected minor axis.

2.3. *Galaxy Spectroscopy*

The galaxy spectra were obtained using the Keck Echelle Spectrograph and Imager, ESI, (Sheinis et al. 2002). The ESI slit position angle was selected to be near the optical major axis of each galaxy in order to accurately measure the galaxy rotation curves. Details of the ESI/Keck observations are presented in Table 2. The ESI slit is $20''$ in length and set to $1''$ wide. We binned by two in the spatial directions resulting in pixel scales of $0.27-0.34''$ over the echelle orders of interest. Binning by two in the spectral direction results in a sampling rate of 22 km s^{-1} pixel^{-1} (FWHM $\sim$ 90 km/s). ESI has a wavelength coverage of 4000 to 10,000 Å, which covers multiple emission lines such as [O II] doublet, Hβ, [O III] doublet, Hα, and [N II] doublet.

All ESI data were reduced using IRAF. Galaxy spectra are both vacuum and heliocentric velocity corrected to provide a direct comparison with the absorption line spectra. The derived wavelength solution was verified against a catalog of known sky-lines which resulted a rms difference of ~ 0.03 Å (~ 2 km s^{-1}).

The galaxy rotation curve extraction was performed following the methods of Kacprzak et al. (2010, 2011a) (also see Vogt et al. 1996; Steidel et al. 2002). We extracted multiple spectra along the spatial direction of a galaxy using three-pixel-wide apertures (corresponding to approximately one resolution element of $0.81-1.02''$ for ESI) at one pixel spatial increments along the slit. To obtain accurate wavelength calibrations, we extract spectra of the arc lines at the same spatial pixels as the extracted galaxy spectra. Fitted arc

TABLE 1
ABSORPTION AND HOST GALAXY PROPERTIES

Quasar field	z_{abs}	z_{gal} [a]	HST Filter	m_{HST} (AB)	log(M_h) ($M_\odot$)	R_{vir} (kpc)	D (kpc)	i (degree)	Φ (degree)	EW_r (Å)	log N(O VI)
quasar sight-lines located along the galaxy's major axis ($\Phi < 25°$)											
J035128.54−142908.7	0.356825	0.356992	F702W	20.7	$12.0^{+0.3}_{-0.2}$	191^{+48}_{-26}	72.3 ± 0.4	$28.5^{+19.8}_{-12.5}$	$4.9^{+33.0}_{-40.2}$	0.396 ± 0.013	14.76 ± 0.17
J091440.39+282330.6	0.244098	0.244312	F814W	19.6	$11.9^{+0.3}_{-0.2}$	171^{+49}_{-24}	105.9 ± 0.1	$39.0^{+0.4}_{-0.2}$	$18.2^{+1.1}_{-1.0}$	0.333 ± 0.028	14.65 ± 0.07
J094331.61+053131.4	0.353286	0.353052	F814W	21.2	$11.7^{+0.4}_{-0.2}$	147^{+54}_{-22}	96.5 ± 0.3	$44.4^{+1.1}_{-1.2}$	$8.2^{+3.0}_{-5.0}$	0.220 ± 0.024	14.66 ± 0.07
J095000.73+483129.3	0.211757	0.211866	F814W	18.0	$12.4^{+0.2}_{-0.2}$	247^{+36}_{-29}	93.6 ± 0.2	$47.7^{+0.1}_{-0.1}$	$16.6^{+0.1}_{-0.1}$	0.211 ± 0.019	14.32 ± 0.04
J104116.16+061016.9	0.441630	0.442173	F702W	20.9	$12.0^{+0.3}_{-0.2}$	193^{+42}_{-25}	56.2 ± 0.3	$49.8^{+7.4}_{-5.2}$	$4.3^{+0.9}_{-1.0}$	0.368 ± 0.023	14.64 ± 0.18
J113910.79−135043.6	0.204297	0.204194	F702W	20.0	$11.7^{+0.4}_{-0.2}$	146^{+52}_{-22}	93.2 ± 0.3	$81.6^{+0.4}_{-0.5}$	$5.8^{+0.4}_{-0.5}$	0.231 ± 0.009	14.40 ± 0.28
J132222.46+464546.1	0.214320	0.214431	F814W	18.6	$12.1^{+0.3}_{-0.2}$	205^{+44}_{-26}	38.6 ± 0.2	$57.9^{+0.1}_{-0.2}$	$13.9^{+0.2}_{-0.2}$	0.354 ± 0.024	14.62 ± 0.12
J134251.60−005345.3	0.227196	0.227042	F814W	18.2	$12.4^{+0.2}_{-0.2}$	252^{+36}_{-29}	35.3 ± 0.2	$10.1^{+0.6}_{-10.1}$	$13.2^{+0.5}_{-0.4}$	0.373 ± 0.023	14.58 ± 0.11
J213135.26−120704.8	0.430164	0.430200	F702W	20.7	$12.0^{+0.3}_{-0.2}$	200^{+42}_{-25}	48.4 ± 0.2	$48.3^{+3.5}_{-3.7}$	$14.9^{+6.0}_{-4.9}$	0.385 ± 0.013	14.60 ± 0.05
J225357.74+160853.6	0.390705	0.390013	F702W	20.6	$12.2^{+0.2}_{-0.2}$	217^{+45}_{-28}	276.3 ± 0.2	$76.1^{+1.1}_{-1.2}$	$24.2^{+1.2}_{-1.2}$	0.173 ± 0.030	14.29 ± 0.04
quasar sight-lines located along the galaxy's minor axis ($\Phi > 33°$)											
J012528.84−000555.9	0.399090	0.398525	F702W	19.7	$12.5^{+0.2}_{-0.2}$	285^{+37}_{-32}	163.0 ± 0.1	$63.2^{+1.7}_{-2.6}$	$73.4^{+4.6}_{-4.7}$	0.817 ± 0.023	15.16 ± 0.04
J045608.92−215909.4	0.381514	0.381511	F702W	20.7	$12.0^{+0.3}_{-0.2}$	192^{+48}_{-26}	103.4 ± 0.3	$57.1^{+19.9}_{-2.4}$	$63.8^{+4.3}_{-2.7}$	0.219 ± 0.013	14.34 ± 0.13
J094331.61+053131.4	0.548769	0.548494	F814W	21.0	$12.0^{+0.3}_{-0.2}$	191^{+43}_{-25}	150.9 ± 0.6	$58.8^{+0.6}_{-1.1}$	$67.2^{+0.9}_{-1.0}$	0.275 ± 0.050	14.51 ± 0.07
J100902.07+071343.9	0.227851	0.227855	F625W	20.1	$11.8^{+0.4}_{-0.2}$	155^{+51}_{-23}	64.0 ± 0.8	$66.3^{+0.6}_{-0.9}$	$89.6^{+1.3}_{-1.3}$	0.576 ± 0.021	15.14 ± 0.10
J113910.79−135043.6	0.212237	0.212259	F702W	20.0	$11.7^{+0.4}_{-0.2}$	150^{+52}_{-22}	174.8 ± 0.1	$85.0^{+0.1}_{-0.6}$	$80.4^{+0.4}_{-0.5}$	0.137 ± 0.009	14.12 ± 0.12
J113910.79−135043.6	0.319167	0.319255	F702W	20.6	$11.9^{+0.3}_{-0.2}$	170^{+51}_{-24}	73.3 ± 0.4	$83.4^{+1.4}_{-1.1}$	$39.1^{+1.9}_{-1.7}$	0.255 ± 0.012	14.41 ± 0.09
J124154.02+572107.3	0.205538	0.205267	F814W	19.9	$11.6^{+0.4}_{-0.2}$	140^{+52}_{-21}	21.1 ± 0.1	$56.4^{+0.3}_{-0.5}$	$77.6^{+0.3}_{-0.4}$	0.519 ± 0.018	14.89 ± 0.13
J155504.39+362847.9	0.189033	0.189201	F814W	18.5	$12.1^{+0.3}_{-0.2}$	194^{+45}_{-25}	33.4 ± 0.1	$51.8^{+0.7}_{-0.7}$	$47.0^{+0.3}_{-0.8}$	0.385 ± 0.033	14.74 ± 0.17
J225357.74+160853.6	0.153821	0.153718	F702W	19.3	$11.6^{+0.5}_{-0.2}$	130^{+53}_{-20}	31.8 ± 0.2	$59.6^{+0.9}_{-1.7}$	$33.3^{+2.7}_{-1.9}$	0.263 ± 0.056	14.59 ± 0.06
J225357.74+160853.6	0.352708	0.352787	F702W	20.3	$11.9^{+0.3}_{-0.2}$	180^{+50}_{-25}	203.2 ± 0.5	$36.7^{+6.9}_{-4.6}$	$88.7^{+4.6}_{-4.8}$	0.381 ± 0.036	14.70 ± 0.15

[a] Keck ESI redshifts derived from this work.

lamp exposures provided a dispersion solution with an RMS of ~ 0.035 Å (~ 2 km s^{-1}). The Gaussian fitting algorithm (FITTER: see Churchill et al. 2000a) was used to compute best-fit emission- and absorption-line centers and widths to derive galaxy redshifts and kinematics. Galaxy redshifts were computed at the velocity centroid of the line, accounting for emission-line resolved kinematics and/or luminosity asymmetries. The galaxy redshifts are listed in Table 1; their accuracy ranges from $3-20$ km s^{-1}. The 20 rotation curves are presented in Appendix A for the 10 quasar sight-lines along the galaxy's major axis (Figures A1–A5) and in Appendix B for the 10 quasar sight-lines along the galaxy's minor axis (Figures B1–B5).

3. RESULTS

In this section, we explore the kinematic relationship between O VI absorption and their host galaxies.

3.1. *Gravitationally Bound OVI*

We first explore whether the O VI CGM gas is gravitationally bound to their host galaxy dark matter halos. In Figure 1, we show the velocity difference between the median optical depth distribution of the O VIλ1031 absorption line and the galaxy systemic velocity as a function of the host galaxy halo mass for all azimuthal angles. The error bars show the full velocity range of the absorption, which is defined as where the Voigt profile fitted absorption models return to 1% from the continuum level. The Voigt profile models are preferred to define the velocity ranges since some O VI absorption systems are blended with other ions in the spectra (see Nielsen et al. 2017) and the data tend to be quite noisy.

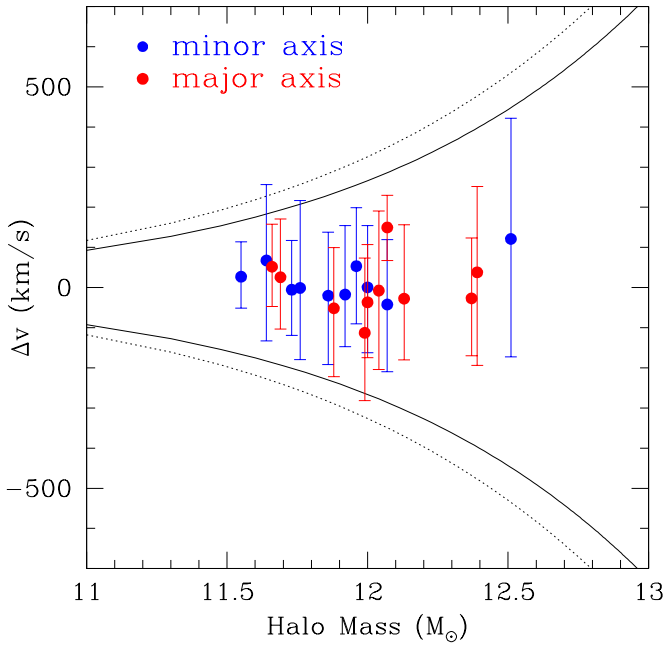

FIG. 1.— The points show the velocity of the median optical depth of O VI absorption with respect to their associated galaxy systemic velocity as a function of the inferred galaxy halo mass. The error-bars indicate the full velocity width of the absorption profiles. Our sample is split into two azimuthal angle bins: major axis (red – $\Phi < 25°$) and minor axis (blue – $\Phi > 33°$). The two curves indicate the halo escape velocities from 100 kpc (dotted) and 200 kpc (solid). Note that almost all O VI absorption has velocities well within the halo escape velocities.

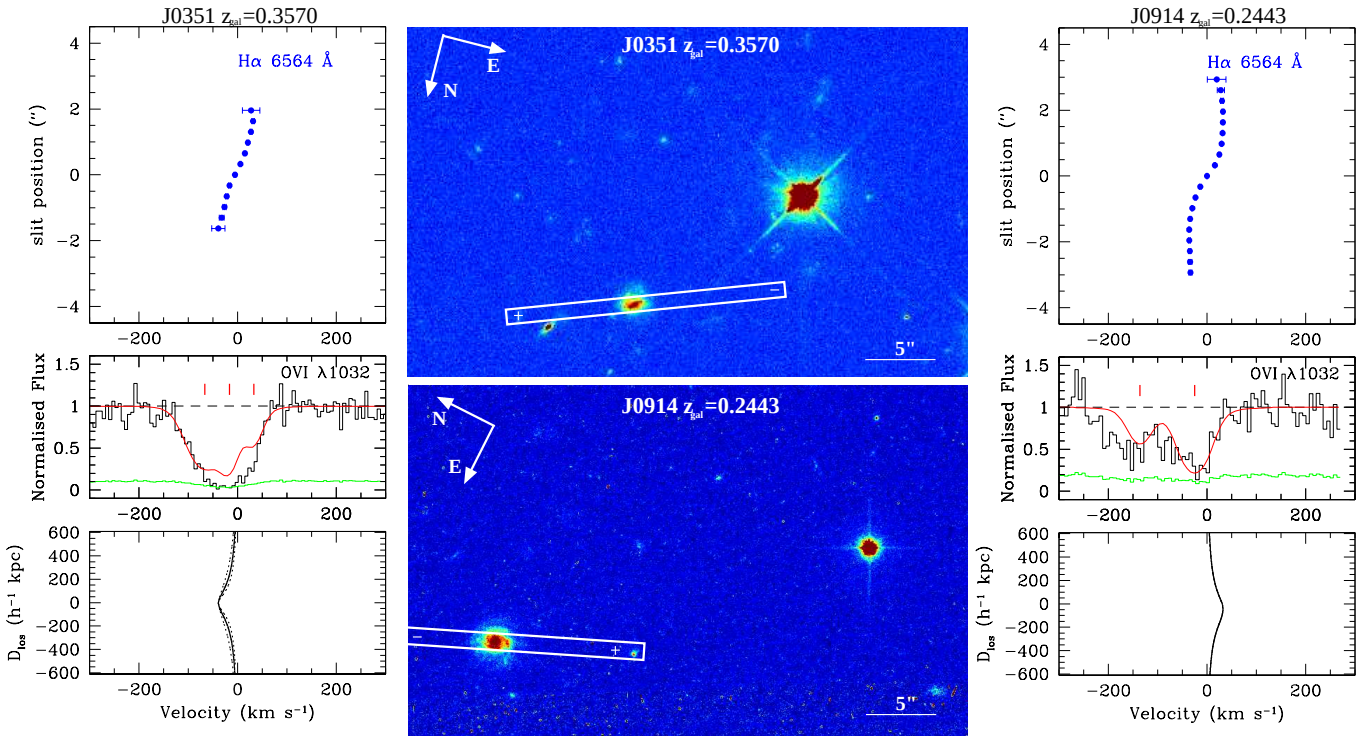

FIG. 2.— *HST* images and galaxy rotation curves presented for two fields where the quasar sight-line aligns with the galaxy's major axis. (Top middle) A $45'' \times 25''$ *HST* image of the quasar field J0351. The ESI/Keck slit is superimposed on the image over the targeted galaxy. The "+" and "−" on the slit indicate slit direction in positive and negative arcseconds where $0''$ is defined at the galaxy center. (Left) The $z = 0.3570$ galaxy rotation curve and the *HST*/COS O VI λ1031 absorption profile is shown with respect to the galaxy systemic velocity. The panel below the O VI absorption is a simple disk rotation model computed using Equation 1, which is a function of the galaxy rotation speed and orientation with respect to the quasar sight-line. The J0351 galaxy is rotating in the same direction as the absorption however, the velocity range covered by the model is not consistent with the entire range covered by the absorption profile. (Bottom middle) Same as top middle except for the J0914 quasar field and for the targeted galaxy at $z = 0.2443$ (Right) Same as left except the $z = 0.2443$ in the J0914 quasar field. Note here that the O VI absorption is consistent with being counter-rotating with respect to the galaxy and again, the model has insufficient velocities to account for all the absorption kinematics. In both cases disk-rotation does not reproduce the observed absorption velocities. Figures for all galaxies are found in Appendix A (major-axis) and Appendix B (minor-axis).

TABLE 2
ESI OBSERVATIONS

Quasar field	z'_{gal}	z'_{gal} ref [a]	Observation date	Slit PA (deg)	Exp (sec)
J012528.84−000555.9	0.3985	3	2014−12−13	15	1800
J035128.54−142908.7	0.3567	1	2014−12−13	110	2550
J045608.92−215909.4	0.3818	1	2014−12−13	110	1200
J091440.39+282330.6	0.2443	2	2016−01−15	23	1500
J094331.61+053131.4	0.3530	2	2016−01−15	38	4500
J094331.61+053131.4	0.5480	2	2016−01−15	−218	4500
J095000.73+483129.3	0.2119	2	2016−01−15	13	1000
J100902.07+071343.9	0.2278	2	2016−01−15	115	1200
J104116.16+061016.9	0.4432	5	2014−04−25	−110	3300
J113910.79−135043.6	0.2044	1	2016−01−15	160	1650
J113910.79−135043.6	0.2123	1	2016−01−15	111	2400
J113910.79−135043.6	0.3191	1	2016−06−06	94	1800
J124154.02+572107.3	0.2053	2	2016−06−06	121	1200
J132222.46+464546.1	0.2142	2	2016−06−06	0	1500
J134251.60−005345.3	0.2270	2	2016−06−06	−24	1800
J155504.39+362847.9	0.1893	2	2016−06−06	130	1800
J213135.26−120704.8	0.4300	6	2015−07−16	55	6000
J225357.74+160853.6	0.1530	1	2015−07−16	−213	3000
J225357.74+160853.6	0.3526	1	2016−06−06	−185	3300
J225357.74+160853.6	0.3900	1	2016−06−06	30	1200

[a] Original galaxy redshift (z'_{gal}) source: 1) Chen et al. (2001), 2) Werk et al. (2012) , 3) Muzahid et al. (2015), 4) Kacprzak et al. (2010), 5) Steidel et al. (2002), 6) Guillemin & Bergeron (1997).

The rest-frame velocity differences between galaxies and their associated O VI absorption has a mean offset of $dv = 9.2 \pm 58.8$ km s^{-1} with standard error of the mean of 13.5 km s^{-1}. This implies that most of the gas resides near the galaxy systemic velocity regardless of its orientation with respect to the host galaxy. Also included in the figure are curves indicating the escape velocity for a given halo mass at an impact parameter of $D = 200$ kpc (inner curve) and 100 kpc (outer curve) at the median redshift of $z = 0.3$. Note that little-to-no absorption resides outside of these curves, indicating that the O VI gas is bound to their dark matter halos. These results are consistent with previous findings showing bound O VI gas (e.g., Tumlinson et al. 2011; Stocke et al. 2013; Mathes et al. 2014).

3.2. *OVI gas kinematics along the galaxy projected major-axis*

Given the observed O VI azimuthal angle bimodality (Kacprzak et al. 2015), our sample can be easily split into two azimuthal angle bins considered as major and minor axis samples. Here we discuss a subset of 10 systems where the O VI absorption is detected within 25 degrees of the galaxy major axis. This major axis azimuthal cut was selected to mimic the Mg II major axis sample of Ho et al. (2017).

We aim to determine if major-axis O VI displays similar co-rotation kinematic signatures as commonly seen for Mg II absorption (e.g., Steidel et al. 2002; Kacprzak et al. 2010; Ho et

al. 2017). In Figure 2, we present the data used in this analysis for two example fields J0351 and J0914. The Figures for the targeted galaxies where the quasar sightline aligns with their major axis are located in Appendix A. Figure 2 shows the O VI host galaxies and the quasars in the *HST* images along with the ESI slit position placed over each galaxy. The figure further shows the Hα-derived galaxy rotation curve, obtained from the ESI spectra, and the *HST*/COS O VI absorption profile. All velocities are shown with respect to the galaxy systemic velocity. Note that the rotation speeds are low ($\sim$50 km s^{-1}), which is expected for these moderately inclined spiral galaxies. For the galaxy in J0351, the O VI absorption profile covers the entire kinematic range of the galaxy rotation curve. As for the galaxy in J0914, the O VI absorption resides mostly to one side of the galaxy systemic velocity as previously seen for Mg II systems. We now explore if co-rotating/lagging disk models can explain the observed CGM kinematics.

Similar to previous works, we apply the simple monolithic halo model from Steidel et al. (2002) to determine whether an extended disk-like rotating gas disk (as commonly seen for Mg II) is able to reproduce the observed O VI absorption velocity spread given the galaxy's rotation speed and relative orientation with respect to the quasar sightline. In summary, model line-of-sight velocities (v_{los}) are a function of the measurable quantities of impact parameter (D), galaxy inclination angle (i), galaxy–quasar position angle (Φ) and the maximum projected galaxy rotation velocity (v_{max}) such that

$$v_{los} = \frac{-v_{max}}{\sqrt{1+\left(\frac{y}{p}\right)^2}} \exp\left\{-\frac{|y-y_\circ|}{h_v \tan i}\right\} \quad \text{where,} \qquad (1)$$

$$y_\circ = \frac{D\sin\Phi}{\cos i} \quad \text{and} \quad p = D\cos\Phi\,,$$

where h_v is a free parameter representing the scale height for the velocity lag of the CGM. Here, we assume a thick disk (h_v = 1000 kpc), which represents the maximum disk/CGM rotation scenario. Assuming a maximum disk rotation model is reasonable given that we do not know how/if the velocity changes with impact parameter and there is little-to-no velocity gradient along the co-rotating gaseous structures within the simulations (e.g., Stewart et al. 2011; Stewart et al. 2013, 2017).

The parameter y is the projected line of sight position above the disk-plane and y_o is the position at the projected disk mid-plane. The distance along the sightline relative to the point where it intersects the projection of the disk mid-plane is $D_{los} = (y - y_o)/\sin i$. Thus, D_{los} = 0 kpc is where the model line-of-sight intersects the projected mid-plane of the galaxy. Please see figure 6 from Steidel et al. (2002) for a visual representation of the model.

Shown in the bottom panels of Figure 2 are the line-of-sight velocities through the halo derived for the geometry of both galaxy–quasar pairs for CGM gas rotating at a maximum velocity set by the rotation curves (solid curves). The dashed curves indicate model velocities derived from uncertainties in i and Φ. In most cases, error values are small such that the dashed curves lie near/on the solid curves. The z = 0.3570 galaxy in the J0351 field has most of the O VI absorption blueward of the galaxy systemic velocity, which agrees with the direction of rotation of the galaxy and thus model halo. However, given the galaxy's moderate inclination, the model is unable to account for the large velocity spread measured for the absorption profile. Similarly, the z = 0.2443 galaxy in the J0914 field also has the majority of the O VI blueward of the galaxy systemic velocity. In this case, the galaxy is consistent with being counter-rotating with respect to the O VI, with this the model again failing to reproduce the observed velocity spread.

Figure 3 shows the O VI $\lambda\lambda$1031, 1037 absorption profiles along with the Voigt profile fits for the 10 galaxies that have quasar sightlines passing within 25 degrees of the host galaxy's projected major axis. The absorption profiles are plotted relative to the host galaxy systemic velocities. Note that the bulk of the gas resides near the galaxy systemic velocity with a relatively large velocity spread. Below the profiles are the modeled co-rotating line-of-sight velocities. It is immediately clear that the absorption profiles have a much higher velocity range than that of the predicted model line-of-sight velocities. Furthermore, only four systems (J0351, J0943, J1041 and J2131) have models that are rotating in the direction of the bulk of the O VI but still fall short of predicting the observed velocities. The z = 0.35 system in the J0943 field is the only system where the observed O VI gas could be explained by disk rotation and/or accretion. Five systems are consistent with counter-rotating O VI absorption relative to their host galaxies (J0914, J0950, J1322, J1342 and J2251). These results are in stark contrast from what has been found for Mg II galaxy-absorption pairs.

Given that the quasar sight-lines are within 25 degrees of the galaxy major axis, we created the top panel of Figure 4 shows the rotation velocities as a function of the projected distance between the galaxies and their quasar sightlines. The rotation curves for each galaxy are orientated such that the quasar sightlines are located along the positive velocity arm of the rotation curves. The O VI is shown with respect to the galaxy systemic velocity and has the same color as plotted for the rotation curve of their host galaxy. The error bars indicate the full extent of the absorption while the shaded region shows the actual absorption profile in velocity space. This allows the reader to see where the bulk of the optical depth is in relation to the galaxy rotation. The white tickmark indicates the optical depth weighted median of the O VI absorption profile.

It can clearly be seen in the top panel of Figure 4 that the majority of O VI is inconsistent with co-rotation and gas accretion models. Most of the gas resides near the galaxy systemic velocity and there is no preference towards the direction of galaxy rotation. It is still plausible that some of the gas could be accreting/co-rotating, however the signature is not strong or is masked by the other kinematics ongoing within the halo. A mean stacked spectrum of all 10 absorption systems is also shown in the top panel, where the O VI absorption almost symmetrically spans the galaxy systemic velocity where the optical depth weighted median of the stacked spectrum is at 2.5 km s^{-1} relative to the galaxy systemic velocity. Furthermore, the O VI profile encompasses the entire rotational dynamics of the galaxies. This is more clearly shown in the middle panel of Figure 4, where all the velocities are normalized to the maximum line-of-sight rotation velocity for each rotation curve and their associated absorption. Almost all of the systems span the entire dynamical range of the galaxy rotation and more. Again, a mean stacked spectrum is also shown and the O VI spans more than twice the full dynamic range of

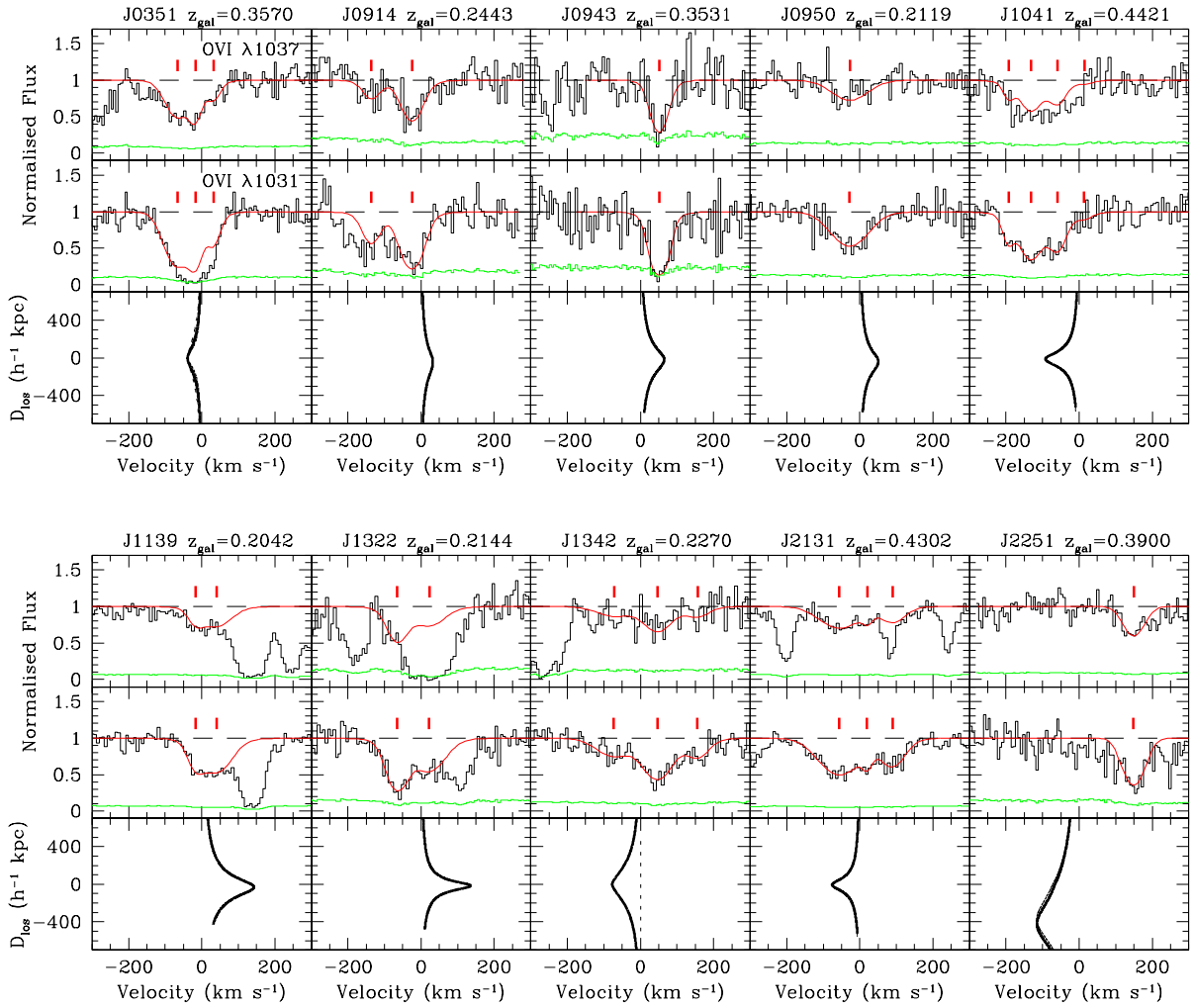

FIG. 3.— O VI λλ1031, 1037 doublet absorption profiles are shown for systems where the quasar sight-line is within 25 degrees of the galaxy major axis. The red line is a fit to the data and the vertical ticks indicate the number of components in each fit. Also shown is the disk model velocities as a function of the distance along the sight-line (D_{los}). D_{los} is equal to zero when the quasar sightline intersects the projected mid-plane of the galaxy. The solid curves are computed using Equations 1 from the values in Table 1. The dashed curves are models computed for the maximum and minimum predicted model velocities given the uncertainties in i and Φ. The disk model is considered successful and reproduces the observations when the solid curve overlaps with the bulk of the absorption kinematics.

the rotation curves. Recall though the O VI gas is still gravationally bound to their halos. The bottom panel in Figure 4 is similar to the middle panel except now shown as a function of viral radius derived for each galaxy. This clearly shows that 9/10 systems are well within the viral radius.

These results indicate that a rotating disk and/or radial infall does not provide a plausible explanation for the total observed O VI kinematics. Thus, this clearly indicates that if there exits a kinematic connection between highly ionized gas and its galaxies, then it is either very low and/or masked by other kinematic sources such as diffuse gas found within the halo. Given that the quasar sight-lines are within < 25 degrees of the galaxy major axes, ongoing outflows would not likely contribute to the absorption kinematics seen here. However, it is possible that recycled gas could could be dominating the observed kinematics.

3.3. *OVI gas kinematics along the galaxy projected minor-axis*

Here we discuss a subset of 10 systems where the O VI absorption is detected at >33 degrees from the galaxy major axis (within 57 degrees of the galaxy minor axis). This angle was selected given that O VI outflowing gas could likely occur within half-opening angles as small as 30 degrees or even larger to 50 degrees (Kacprzak et al. 2015). Figures B1–B5 show the *HST* images along with the galaxy rotation curves and their corresponding O VI absorption. Inspection of these figures shows that the absorption spans the entire galaxy systemic velocity and encompasses the full galaxy rotation velocity range in 4/10 cases while 6/10 systems have most of the O VI absorption offset to one side of the galaxy systemic velocity.

Previous studies have shown that have Mg II galaxy-absorber pairs that disk-like rotation can be found for quasar sightlines with intermediate-to-high Φ values (e.g., Kacprzak et al. 2010). We explore the disk-like rotation model from Equations 1 for our minor axis sample in Figure 5. In Figure 5, the fitted O VI doublet is shown along with the mod-

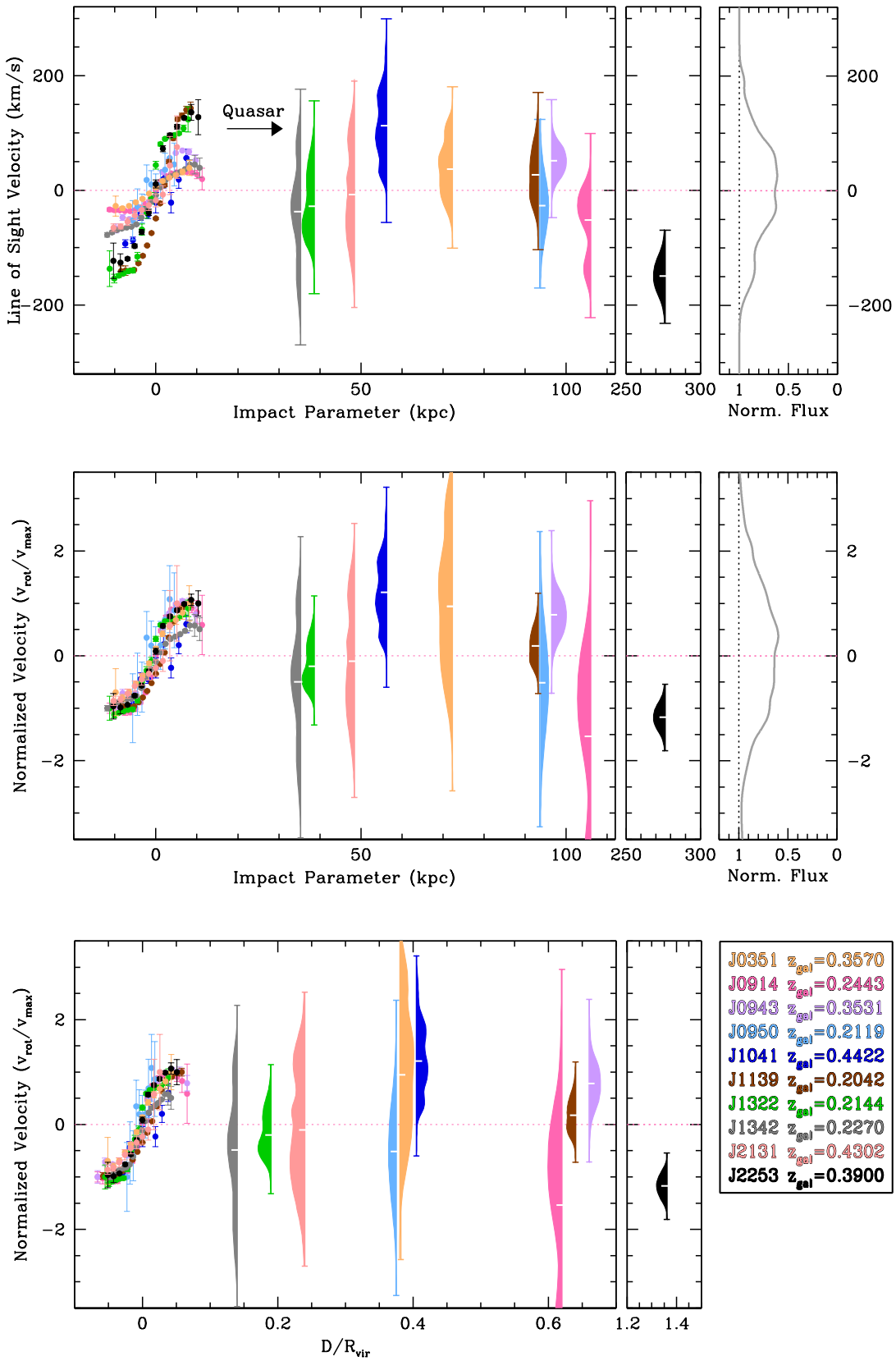

FIG. 4.— (Top) Rotation curves for galaxies where the quasar sightline probes within 25 degrees of the galaxy projected major axis as a function of impact parameter. The rotation curves are orientated such that quasar is probing gas along the positive velocity side of the galaxy. Each galaxy is colored according to the key, which is matched with its corresponding absorption profile. The O VI is shown with respect to the galaxy systemic velocity and the error bars indicate the full extent of the absorption while the shaded region shows the optical depth distribution of the actual absorption profile in velocity space. The white tickmark on the profile indicates the O VI absorption optical depth weighted median velocity. Also shown on the right is the average spectrum of the 10 absorption profiles. The O VI absorption spans the entire velocity range of the galaxy while being centered close to the systemic velocity. (Middle) Same as top except that the galaxy rotation and absorption velocities are now normalized to the peak velocity of each rotation curve. Note that the absorption spans twice the dynamical range of the galaxies. (Bottom) Same as middle except as a function of the ratio of the impact parameter and the inferred halo viral radius.

eled line-of-sight velocities through the halo derived for each galaxy using the maximum velocity set by the rotation curves (solid curves). We find three systems (J1241, J0943 and J1555) where the model can account for all the observed absorption velocities. However, 7/10 have model kinematics consistent with counter-rotation with respect to the bulk of the O VI absorption. What these models demonstrate is that there is not an overall consistency between the relative O VI-galaxy kinematics. Only 4/20 from the total sample of major and minor axis galaxies have relative velocities expected of disk-like rotation/gas accretion. This is in stark contrast to the commonly observed co-rotation found for Mg II absorption.

Given the relative quasar-galaxy geometry, it could be expected that outflows might be commonly observed along the galaxy minor axis. Furthermore, this outflowing gas is likely traced by warm O VI absorption. To test this, we apply a simple conical model for outflowing gas from Gauthier & Chen (2012). Here we summarize the model but see Gauthier & Chen (2012) for details and their figure 1 for an illustration of the model.

Their collimated outflow model is characterized by an expanding cone originating from the galaxy center along the polar axis with a total angular span of $2\theta_0$. As with the disk-rotation model, i is the inclination of the galaxy while Φ is the angle between the projected major axis of the disk and the quasar sightline that is at an impact parameter D. These measured quantities are found in Table 1. The quasar line-of-sight intercepts the outer-edges of the outflow cone at a height z from z_1 to z_2, which is determined by the cone opening angle θ_0. The position angles, $\phi_{[1,2]}$, of the projected outflow cross-section at $z_{[1,2]}$ are constrained by

$$\tan\phi_{[1,2]} = \frac{D\sin\alpha - z_{[1,2]}\sin i}{D\cos\alpha} \quad (2)$$

and the relation between $z_{[1,2]}$ and the opening angle θ_0 is

$$z_{[1,2]}\tan\theta_0 = D\sqrt{1+\sin^2\phi_{[1,2]}\tan^2 i}\left(\frac{\cos\Phi}{\cos\phi_{[1,2]}}\right). \quad (3)$$

Equations 2–3 can be used to calculate the corresponding θ at any given point along the quasar sightline at height z where $z_1 \leq z \leq z_2$.

The ouflow speed, v, of a gas cloud moving outward at a hight z corresponds to the line-of-sight velocity $v_{\rm los}$ such that

$$v = \frac{v_{\rm los}}{\cos j}, \text{ where } j = \sin^{-1}\left(\frac{D}{z}\cos\theta\right). \quad (4)$$

The line-of-sight velocities are defined by the red-most and blue-most velocity edges of the absorption profile relative to the galaxy systemic velocity. The gas producing the observed absorption is assumed to be distributed symmetrically around the polar axis of the cone and the absorption at z_1 and z_2 probes regions close to the front and back side of the outflow respectively. If asymmetry arises due to inhomogeneities of gas with the outflows, then the computed velocity gradients represent a lower limit to outflow velocity field.

We apply the above model since our observational data of the galaxy-quasar geometry provides constraints on θ_0 and the absorption profiles constrain the plausible outflow velocities. From these data, we can identify whether or not reasonable opening angles and outflow velocities are able to replicate the observations. If so, then outflows are a plausible explanation for the observed kinematics, and if not, then outflows may not be the likely source driving the O VI gas kinematics seen along the galaxy minor axis.

Figure 5 shows the outflow models for each quasar-galaxy pair for their relative orientation and absorption gas-galaxy kinematics. The right top panel for each system shows at what height the quasar sightline enters the outflow cone (blue – dash and full lines) and what height the sight-line exits the cone (red – dash and full lines) as a function of outflow opening angle. The Figure shows scenarios where the opening angle is not well constrained, as seen for J1139_0.2123, since the galaxy is nearly edge-on (i = 85 degrees) and the quasar sightline almost directly along the minor axis (within 9.6 degrees). The other scenario shown is for galaxies where the quasar sight-line is not directly along the galaxy minor axis and the outflow opening angle has to be sufficiently large enough before it intercepts the sight-line. This can be seen for J1139_0.3193 (Φ = 39 degrees) and for J2253_0.1537 (Φ = 33 degrees) where the opening has to be at least 50 degrees before the sight-line intercepts the cone.

In all cases, the opening angle on both sides of the cone can be large enough such that the quasar sightline no longer intercepts the cone, which is why z asymptotes to large values. We use the far side of the cone (red) as an upper limit on the outflow half opening angle. From geometric arguments only, the model constrains the half opening angles to range from 0–50 degrees as the smallest possible angle to 26–83 degrees at its largest. The half opening angle model results are presented in Table 3. These are consistent with expected/modeled values found for cooler gas tracers, which range between 10–70 degrees (Walter et al. 2002; Gauthier & Chen 2012; Kacprzak et al. 2012a; Martin et al. 2012; Bordoloi et al. 2014). These are also consistent with those derived by Kacprzak et al. (2015) who examined the azimuthal angle dependence of the gas covering fraction and concluded that the O VI outflowing gas could occur within a half-opening angle as small as 30° or even larger at 50°.

If realistic outflow velocities can reproduce the observed absorption, it would be a key step for understanding whether outflows can explain the observed OVI gas-galaxy kinematics. The bottom panels in Figure 5 show the model outflow velocities at the edges of the cones required to reproduce the entire velocity spread of the observed O VI absorption profile with respect to the galaxy systemic velocity. The blue line corresponds to the outflow velocities where the quasar sightline enters the outflow cone, while the red line corresponds to the outflow velocities where the quasar sightline exits the outflow cone. Each galaxy-absorber pair has a large range of modeled velocities as a function of opening angle required to reproduce the observed line-of-sight velocities. Some of these velocities far exceed 1000 km s^{-1} as the dot product of the outflow velocity vector and the line-of-sight velocity vector approaches zero. Here we assume that the outflow velocities at large distances above the galaxy disk likely do not exceed 1000 km s^{-1} for these systems. This assumption provides additional constraints on the acceptable outflow geometry indicated by the solid line and those values are listed in Table 3. While the range in opening angles is more limited, the viable half-opening angles are still consistent with previous works.

The ranges of the outflows velocities required to reproduce the observed O VI kinematics shown on Figure 5 appear reasonable and are within a few hundred km s^{-1} – typical of expected outflow velocities (e.g., Martin & Bouché 2009; Weiner et al. 2009; Bouché et al. 2012; Gauthier & Chen

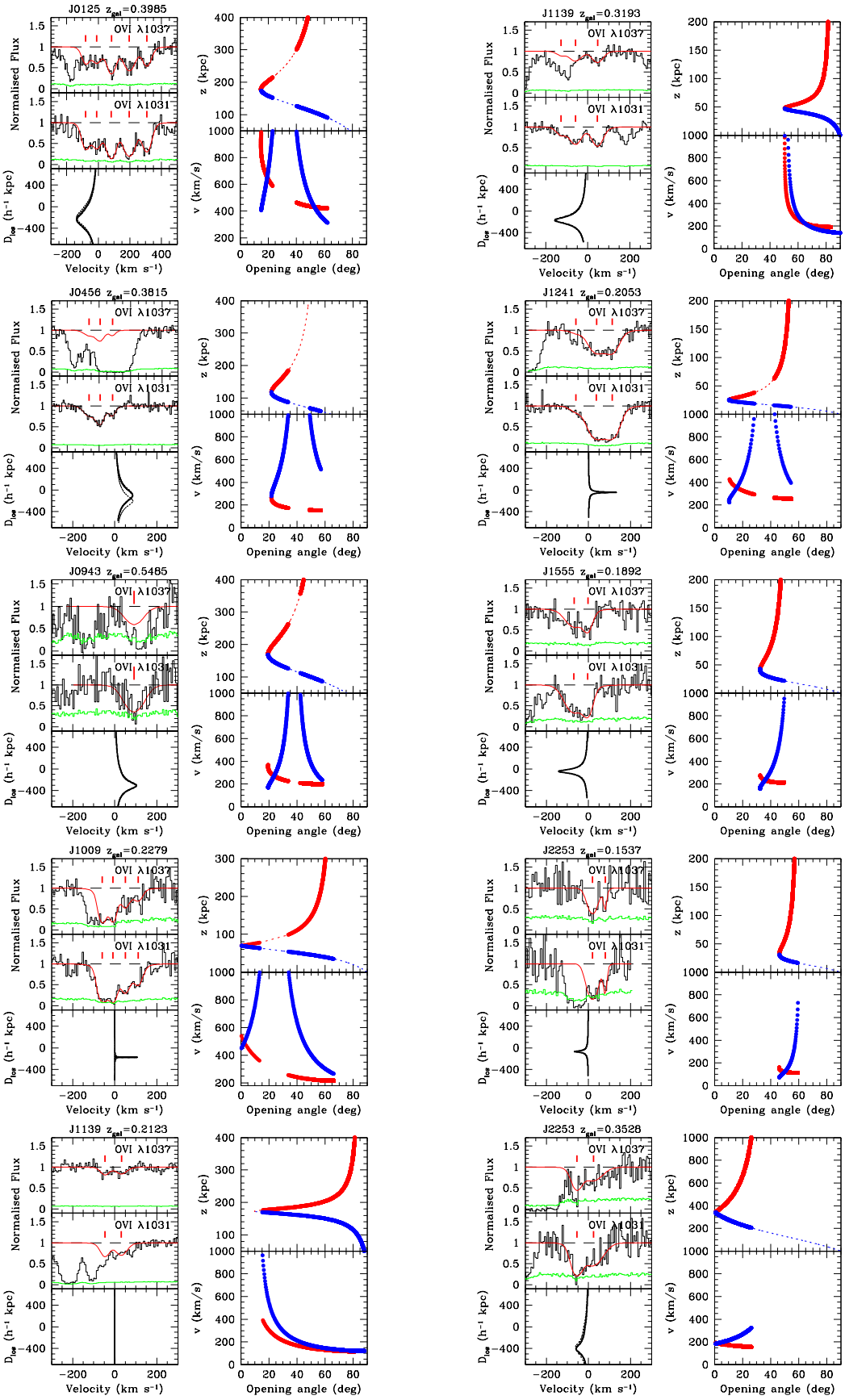

FIG. 5.— (Left) O VI $\lambda\lambda$1031, 1037 doublet absorption profiles shown for systems where the quasar sight-line is within 57 degrees of the galaxy minor axis ($\Phi > 33$ degrees). The red line is the Voigt profile best fit and the vertical ticks indicate the number of components. The panels below the profiles are the disk model velocities as a function of the distance along the sight-line (D_{los}) computed using Equations 1 from the values in Table 1. The solid and dashed curves are computed for the maximum and minimum predicted model velocities given the uncertainties in i and Φ. The model is considered successful when the solid curve overlaps with the bulk of the absorption kinematics. (Right) Outflow models from Equations 2–3 showing the allowed parameter space of the z-height (top) and outflow velocities (bottom) versus the half opening angle. The colored lines highlight the height at which the sight lines enter (blue) and leave (red) the outflow. If we assume that the line-of-sight velocity increases smoothly from z_1 to z_2, then outflows accelerate, as seen in the lower velocity panel, when the blue line is below the red line and decelerate when the red line is below the blue line.

2012; Martin et al. 2012; Rubin et al. 2014; Schroetter et al. 2016). We emphasize, however, that a modeled active accelerating outflow occurs when the line-of-sight velocity increases from where the quasar sightline enters the conical outflow to where the quasar sightline exits the conical outflow (since $z_1 < z_2$). The outflow velocities (v) shown in Figure 5 would be consistent with an active outflowing model when the blue line is below the red line. In the opposite case, where the red line is below the blue line, the outflow is decelerating in order to reproduce the observed kinematics.

We find that 7/10 galaxies exhibit outflowing gas with an accelerated flow. Note however, that acceleration only occurs for very small opening angles typically within 20 degrees and only over a range of 10 degrees (with the exception of J1139_0.3193). These values are also listed in Table 3. Thus, if active outflows are occurring, they only occur within a very small opening angle conical outflow.

For the majority of the opening angle range, the outflow velocities required to reproduce the observations would be decelerating as the gas moves further away from the host galaxy. With the assumed velocity cut of 1000 km s^{-1}, there still remains a large range of opening angles that are valid (see Table 3). This would imply that either active outflows exist, and at these large heights above the disk, the gas is rapidly decelerating or the absorption is a result of previously ejected gas that is potentially falling back onto the galaxy.

A caveat of these models is that we have assumed that all of the gas seen in absorption is a result of the outflow. If only some fraction of the gas is associated with outflows, then the model velocities, and where acceleration and deceleration occur, would be different and likely are expressed as upper limits. However, we do not have any evidence to counter this assumption. Thus, we find that accelerating outflow gas can only occur over a very small range of opening angles and most of the time the gas is found to be decelerating.

4. AMR COSMOLOGICAL SIMULATIONS

We use cosmological simulations to provide further insight into what mechanisms are driving the observed O VI velocity spread. These hydrodynamical simulations provide the theoretical means to fully incorporate dynamical processes, such as accretion and outflows, in a cosmological setting. We apply the method of quasar absorption lines to the simulations to observe the O VI absorption kinematics. Here we analyze eight $z = 1$ simulated galaxies to identify the possible structures and mechanisms that give rise to the observed O VI halo gas kinematics.

4.1. *Description of The Simulations*

We analyzed ΛCDM cosmological simulations created using the Eulerian Gasdynamics plus N–body Adaptive Refinement Tree (ART) code (Kravtsov 1999, 2003). The zoom-in technique (Klypin et al. 2001) applied here allows us to resolve the formation of single galaxies consistently in their full cosmological context.

We analyzed the VELA simulation suite (Ceverino et al. 2014; Zolotov et al. 2015), which were created to compliment the *HST* CANDELS survey (Barro et al. 2013, 2014). The hydrodynamic code used to simulate these galaxies incorporates prescriptions for star formation, stellar feedback, supernovae type II and Ia metal enrichment, radiation pressure, self-consistent advection of metals, and metallicity-dependent cooling and photo-ionization heating due to a cosmological ultraviolet background. Our simulations have a feedback model, named RadPre_LS_IR (Ceverino et al. 2014), that differs from previous studies (Zolotov et al. 2015). This model includes radiation pressure from infrared photons, as well as photoheating/photoionization around young and massive stars. Further details regarding the various models included in these simulations can be found in (Ceverino & Klypin 2009) and (Ceverino et al. 2014).

These simulations resulted in a maximum spatial resolution of 17 pc, a dark matter particle mass of 8×10^4 M$_\odot$, and a minimum stellar particle mass of 10^3 M$_\odot$. The high resolution implemented in the VELA simulations allow us to resolve the regime in which stellar feedback overcomes the radiative cooling (Ceverino & Klypin 2009), which results in naturally produced galactic scale outflows (Ceverino et al. 2010, 2016). Thus, galaxy formation proceeds in a more realistic way through a combination of cold flow accretion, mergers, and galaxy outflows.

Here we select a subsample of the VELA galaxies which a) were evolved to the lowest redshift of $z = 1$, b) did not experience a major merger near $z = 1$, and c) have a virial mass range between log M$_{vir}$ = 11.3 – 12 (see Table 4 for halo virial quantities). The selection resulted in 8 galaxies having an average log M$_{vir}$ = 11.7 ± 0.2 M$_\odot$ and log M$_*$ = 10.5 ± 0.3 M$_\odot$.

4.2. *Simulated Spectra*

We employed the HARTRATE photo+collisional ionization code (Churchill et al. 2014) that is optimally designed to model optically thin gas with no ionization structure. For the vast majority of the CGM, including the O VI column densities and impact parameters studied here, this is a safe assumption. The consequence of not including any optical depth considerations is that HARTRATE may under-predict ions that typically reside in optically thick conditions (such as Mg II), however, this is not a concern here since this assumption only breaks down close to central galaxies or near satellite galaxies. A proper treatment of the radiation field would require computationally intensive full radiative transfer computations, which is beyond the scope of this work.

In summary, HARTRATE incorporates photo-ionization, direct collisional ionization, Auger ionization, excitation-autoionization, photo-recombination, high/low temperature dielectronic recombination, charge transfer ionization by H^+, and charge transfer recombination by H^0 and He^0. HARTRATE uses solar abundance mass fractions (Draine 2011; Asplund et al. 2009), a Haardt & Madau (2012) ionizing spectrum is used for the ultraviolet background and assumes ionization equilibrium. The cosmological simulations provides HARTRATE with the hydrogen number density, kinetic temperature and the gas metallicity (i.e., supernovae type II and Ia yields). The outputs from HARTRATE include the electron density, the ionization and recombination rate coefficients, ionization fractions and the number densities for all ionic species up to zinc. The software has been applied successfully in previous works (Kacprzak et al. 2012b; Churchill et al. 2012, 2015) and see Churchill et al. (2014) for details on the code and its successful comparisons to Cloudy.

The methodology of producing mock observations of quasar sightlines through the cosmological simulations is described in detail in Churchill et al. (2015) and Vander Vliet (2017). The outputs from HARTRATE are applied to Mockspec, which performed the mock quasar absorption analysis.

TABLE 3
MODEL OUTFLOW HALF OPENING ANGLES AND VELOCITIES

Quasar field	z_{abs}	$z(i)$ [a] (kpc)	$v_{red}(i)$ [b] (km s^{-1})	$v_{blue}(i)$ [c] (km s^{-1})	θ (deg.) [d] (geometric)	θ (deg.) [e] (velocity limited)	θ (deg.) [f] (acceleration only)
J012528.84–000555.9	0.398525	174	991	406	15–62	15–23 & 40.1–62	15–19
J045608.92–215909.4	0.381511	118	266	279	22–57	22–34 & 49.0–57	–
J094331.61+053131.4	0.548494	169	369	168	19–58	19–34 & 42.4–58	19–23
J100902.07+071343.9	0.227855	70	540	450	0–66	0–14 & 33.8–66	0–3
J113910.79–135043.6	0.212259	172	>1000	>1000	10–81	15–81	–
J113910.79–135043.6	0.319255	47	>1000	996	50–83	53–83	65–83
J124154.02+572107.3	0.205267	26	428	223	11–55	11–29 & 42–55	11–16
J155504.39+362847.9	0.189201	43	277	158	33–50	33–50	33–36
J225357.74+160853.6	0.153718	31	162	74	46–60	46–60	46–50
J225357.74+160853.6	0.352787	342	192	184	1–26	1–26	–

[a] The height about the disk.
[b] The velocity of the red side of the cone at the lowest value of the opening angle.
[c] The velocity of the blue side of the cone at the lowest value of the opening angle.
[d] The half opening angle constrained by geometric arguments only.
[e] The half opening angle constrained by geometric arguments and for velocites less than 1000 km s^{-1}.
[f] Half opening angles where accelerated outflows exist.

TABLE 4
PROPERTIES OF $z = 1$ VELA GALAXIES

VELA Galaxy	$\log(M_{vir}/M_\odot)$	$\log(M_*/M_\odot)$	R_{vir} (kpc)
21	12.0	10.9	151
22	11.8	10.7	133
23	11.7	10.4	118
25	11.5	10.2	103
26	11.6	10.4	112
27	11.6	10.3	110
28	11.3	9.9	92
29	12.0	10.6	146

Mockspec is publicly available in a GitHub repository[7]. We ran HARTRATE on a smaller box size of 6 R_{vir} along a side centered on the dark matter halo of the host galaxy and drew 1000 lines of sight within a maximum impact parameter of 1.5 R_{vir}.

Absorption spectra with the instrumental and noise characteristics are generated assuming each cell gives rise to a Voigt profile at its line of sight redshift. The mock quasar sightline is then objectively analyzed for absorption above the equivalent width threshold of 0.02 Å, which corresponds to $\log N(\mathrm{O\,VI}) = 13.55$ cm^{-2} for $b = 10$ km s^{-1}. The optical depth weighted median redshifts, rest–frame equivalent widths and velocity widths and column densities are then measured from the spectra (see Churchill & Vogt 2001). The velocity zero point of the simulated absorption lines is set to the line of sight velocity of the simulated galaxy (center of mass of the stars). For this analysis, all the eight simulated galaxies are analyzed with the disk appearing edge-on to the observer. The galaxy inclination is determined relative to the angular moment vector of cold gas ($T < 10^4$ K) within 1/10 of R_{vir}. The systemic velocity of the galaxy is determined by the dark matter particles within the halo virial radius.

To examine the spatial and kinematic properties of gas giving rise to OVI absorption, we identify OVI absorbing gas cells along each sightline as those which contribute to detected absorption in the simulated spectra. The gas cells along the sightline are sorted into decreasing column density and the lowest are systematically removed until the noiseless spectrum created by the remaining cells has an equivalent width that is 95% of the equivalent width of the original spectrum.

[7] https://github.com/jrvliet/mockspec

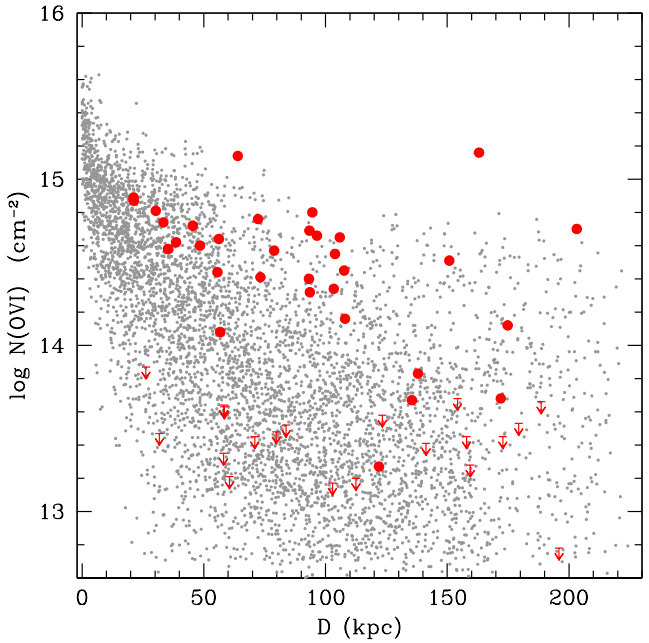

FIG. 6.— OVI column densities are shown as a function of impact parameter. Red points are observations taken from Kacprzak et al. (2015). Grey points are from mock sightlines around 8 simulated galaxies as described in the text.

4.3. *Results Derived From Simulations*

In Figure 6, we show the OVI column density distribution from the simulations (grey) and from the observations of Kacprzak et al. (2015) (red). We note an anti-correlation for both the observations and simulations between the column density and impact parameter. There is overlap between the simulated and observe column densities, while also being consistent with previous works using simulations (Hummels

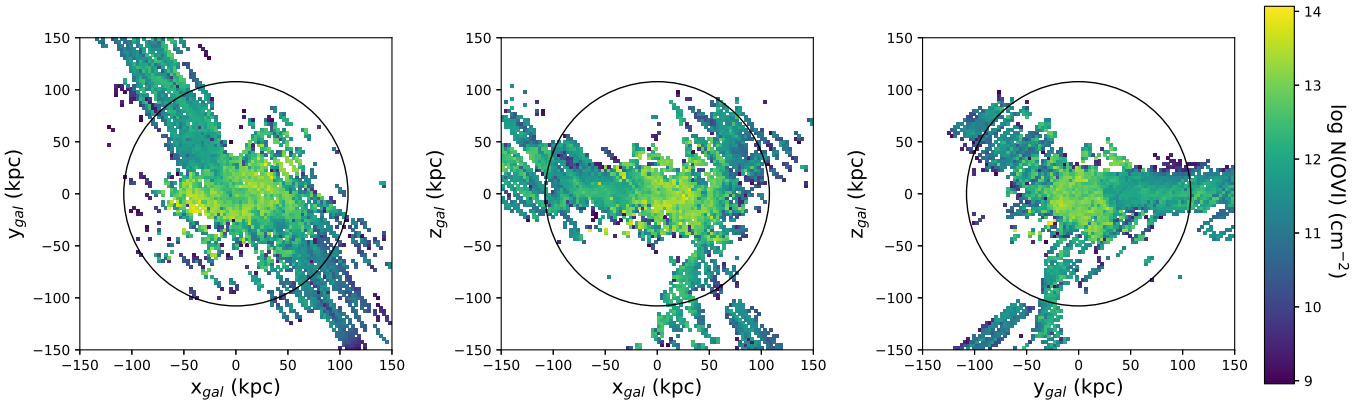

FIG. 7.— Median O VI column density spatial distribution located along sightlines drawn through an example simulated galaxy. The coordinate system is defined so the disk lies in the *xy*-plane with the angular moment vector of cold gas along the positive *z* axis. O VI absorption cells are shown for those that contribute to the absorption profiles (see text for methodology). The black circle shows the virial radius. Note 2–3 large filament structures that extend beyond 150 kpc around the galaxy. The O VI within the central 40 kpc of the galaxy has a roughly spherical distribution.

et al. 2013; Ford et al. 2016; Liang et al. 2016; Oppenheimer et al. 2016; Gutcke et al. 2017; Suresh et al. 2017). Although the simulations shows a larger degree of scatter, which coud be driven by galaxy inclination, etc., they can still provide useful insight into the kinematics driving the existence of O VI systems. We will explore this scatter and offsets between observations and simulations in an upcoming paper.

Figure 7 shows the median O VI column density distribution for sightlines through the simulations for a single example galaxy of VELA 27. Only the cells contributing the the O VI absorption (as described in the previous section) are shown. The coordinate system for the example galaxy is defined so the disk lies in the *xy*-plane with the angular moment vector of cold gas along the positive *z* axis. The black circle indicates the virial radius. A somewhat spherical O VI halo is present within ∼40-50 kpc of the galaxy center and has almost unity covering fraction. This spherical halo around the host galaxy has column densities ranging between log N(O VI)= 12.5 − 14.

Beyond 50 kpc are possibly three thick filaments responsible for producing the high impact parameter absorption with column densities decreasing to log N(O VI)= 12.5 − 11. These two features, halos and streams, are seen in all of our simulated galaxies. Note that in this particular example galaxy that the filaments are not co-planer and tend to be in different locations for all galaxies. We will explore the spatial distribution of O VI in an upcoming paper. Next we examine whether these structures in the simulations are able to reproduce the typical absorption profiles and kinematics seen in our observations.

Figure 8 shows the same O VI gas cells contributing to the absorption profiles as seen in Figure 7, but now color-coded as a function of velocity in spherical coordinates v_r, v_θ and v_ϕ. Here the median velocity of all the O VI cells contributing to the absorption along each projection of the sightlines are shown.

The top panel has the radial velocity component showing what speeds the O VI gas is traveling directly away or towards the center of the galaxy. It can be clearly seen that there is significant radial inflow towards the galaxy center along the filament structures. In this particular example, the inflowing gas appears to have a roughly constant velocity ranging between −150 to −200 km s^{-1}, with potentially an increase towards the galaxy center. The central part of the galaxy halo has a component that exhibits slower inflow velocities of 0–100 km s^{-1} that sits both near and outside of the filaments. Most of the gas near the galaxy averages along the line of sight is close to the systemic velocity. We see only a few gas cells in this example that have positive, radially outflowing, velocities ranging from 0–100 km s^{-1}.

The middle panel shows v_θ, which is the rotation velocity, where gas co-rotating with the galaxy has positive speeds and gas counter-rotating with the galaxy is galaxy has negative velocities. In the inner 50 kpc, the gas is rotating in the same direction as the galaxy having velocities between 50–100 km s^{-1}. This co-rotating gas appears to be in the same plane as the edge-on disk galaxy, suggesting some connection between the O VI and disk gas. There is also some gas within 50 kpc that is near the systemic velocity and some counter-rotating with speeds < 50 km s^{-1}. Beyond 50 kpc, most of the gas showing little sign of rotation while some gas is counter-rotating with a range of velocities from 0 to −150 km s^{-1}. The dominant velocity component outside of 50 kpc is the radial component.

The last panel shows v_ϕ, which is the rate of change of the angle between the vector to the gas cell and the *z*–axis, which is aligned with the galaxy's angular momentum vector. In the central region, we see positive velocities which decrease closer to systemic velocity with increasing impact parameter. There are some negative velocities out in the filaments as well.

We next explore the 8 simulations in a statistical sense in order to determine general kinematic trends and origins of the O VI CGM.

The top panel of Figure 9 shows the mean stacked Voigt profile fits to the O VI that is located along the galaxy major ($\Phi < 25°$) and minor ($\Phi < 33°$) axes for our observations. Note both have similar kinematic shape and are centered near the galaxy systemic velocity. The major axis gas is offset by 2.5 km s^{-1} from the galaxy systemic velocity while the minor axis gas is offset by 28.0 km s^{-1} from the galaxy systemic velocity. This implies that there are no strong kinematic signatures present if outflows and accretion are traced by O VI gas, or outflow and accretion signatures could be hidden by a larger diffuse collection of O VI within the halo at similar velocities.

To compare our observations to the simulations, we select all absorption systems from the 8 simulated galaxies that have

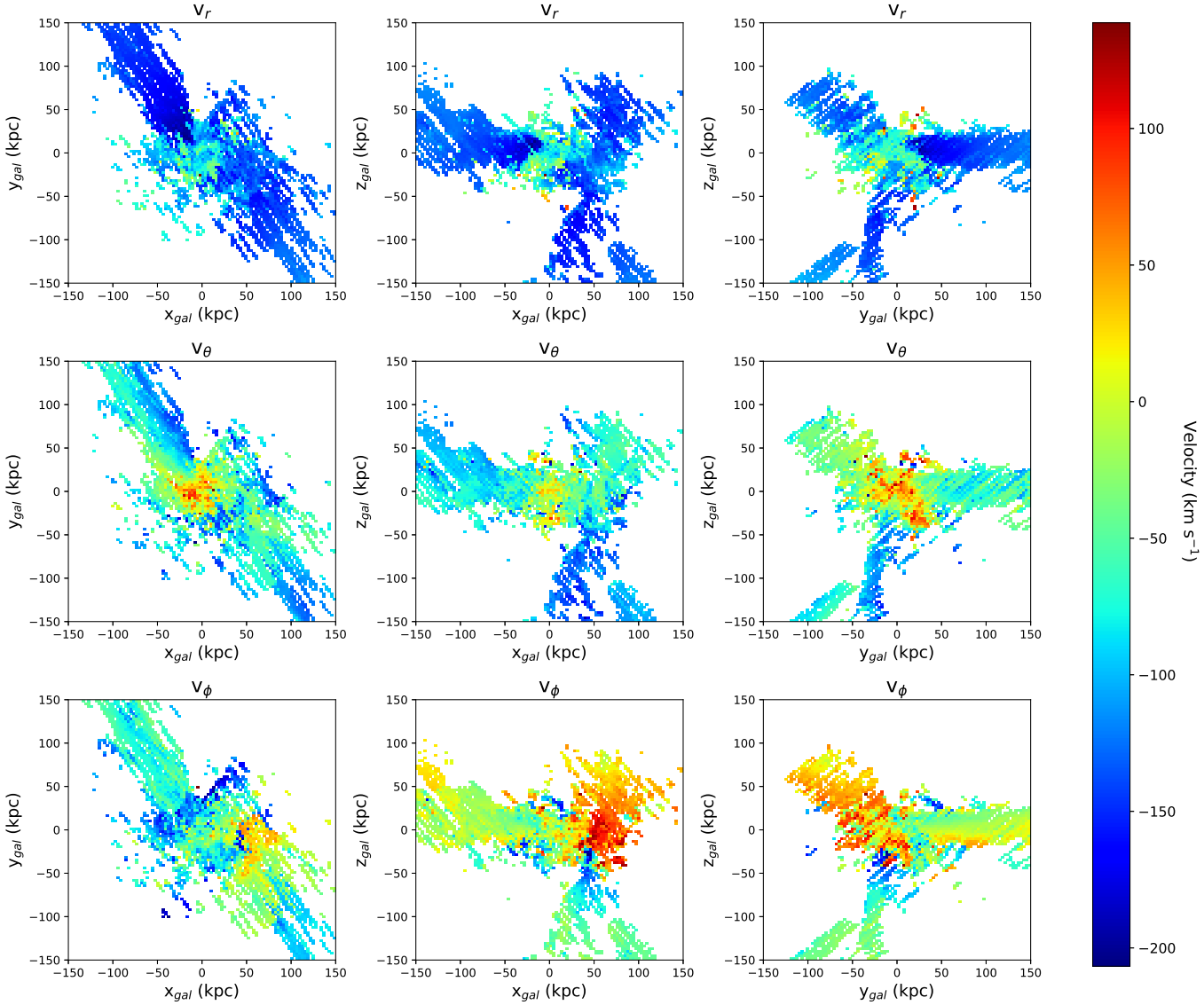

FIG. 8.— The OVI spatial distribution located along sightlines drawn through an example simulated galaxy. The coordinate system is defined so the galaxy disk lies in the xy-plane with the angular moment vector of cold gas along the positive z axis. OVI absorption cells are shown for those that contribute to the absorption profile (see text). OVI gas cells are color-coded by the median velocity along the projection in spatial coordinates (Top) v_r, (Middle) v_θ and (Bottom) v_ϕ. For v_θ, positive velocities indicates gas co-rotation with the same direction as the galaxy, which occurs for OVI gas within 25 kpc of this example galaxy. Note both the significant radial inflow along the filaments and the co-rotating OVI near the galaxy disk.

an equivalent width larger than 0.2 Å, which is roughly the observational limit of our sample. For the simulations, major axis gas is defined as having an azimuthal angle less than 30 degrees, while minor axis gas has an azimuthal angle greater than 40 degrees. These absorption systems were then combined to provide the mean stacked spectra shown in Figure 9. We note that the optical depths and the velocity spread between the simulations and observations are similar, with some differences with the kinematic shape of the profile.

The OVI found near the major axis in the simulations exhibits a possible bimodal distribution with bulk of the absorption residing near $100-125$ km s^{-1} of each side of the galaxy systemic velocity. This signature is reminiscent of co-rotation/accretion predictions (Stewart et al. 2011; Stewart et al. 2013; Danovich et al. 2015; Stewart et al. 2017). OVI found near the minor axis in the simulations exhibits an offset of ~ 50 km s^{-1} from the galaxy systemic velocity but has a similar velocity spread to the observations. The simulated mean stacked spectra do show some hints of kinematic structures, such as rotation along the major axis, which does differ from our observations. This could be due to only having 10 sight-lines from our observations, or differences due to inclination angle effects. We next examine the typical OVI velocities to determine what is driving the OVI kinematic distribution within the simulations.

Figure 10, shows the median OVI cell velocities averaged over the eight simulations shown for gas along the major (red) and minor (blue) axis. The first panel shows the radial velocity component for major and minor axis gas along with the standard error in the mean. Gas along the major axis of the galaxy appears to inflow towards the galaxy at high velocities at high impact parameter and slows to the galaxy systemic

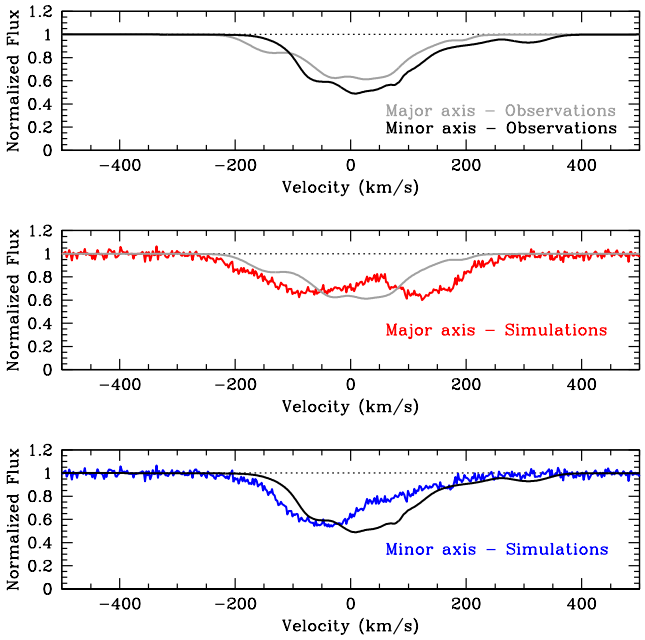

FIG. 9.— (Top) Average observational O VI spectra of 10 sightlines along both the major (grey) and minor (black) axes of our sample (see Section 3). Both absorption profiles have similar line shapes and kinematics and are centered near the galaxy systemic velocity. (Middle) Observational O VI major axis average spectrum shown along with the average spectrum from the simulations for major axis O VI absorption. The simulated galaxy major axis is defined as having an azimuthal angle less than 30 degrees with absorption systems with equivalent widths of > 0.2 Å. The simulated spectra were computed using all sightlines along the major axis of all 8 simulated galaxies. (Bottom) Observational O VI minor axis average spectrum shown along with the average spectrum from the simulations for minor axis gas having an azimuthal angle greater than 40 degrees for absorption systems having equivalent widths of > 0.2 Å. Note the similar optical depths between the observations and simulations, while they differ in their kinematic profiles.

velocity as it approaches the galaxy center. The largest deceleration occurs within 50 kpc, reducing in speed from −50 to 0 km s^{-1}. Thus, both Figures 8 and 10 indicate that O VI gas does inflow along filaments and decelerating as it approaches the galaxy.

On the other-hand, minor axis O VI is outflowing out to about 50 kpc, then it decelerates and falls back towards the galaxy. The minor axis gas has similar radial velocities as the major axis gas beyond 75 kpc, which would make it difficult to identify the difference between accreting and re-accreted gas. Thus, outflows traced by O VI only influence the CGM out to 50 kpc for a Milky Way-like galaxy and recycled outflows, which are a common prediction from simulations as an origin of O VI gas, dominate at higher impact parameters. This is consistent with the toy outflow models in Section 3.3, indicating that if the gas is originating from outflows, the gas has to be decelerating and possibly falling back to the galaxy. Furthermore, our minor axis observational sample contains 3 galaxies with impact parameters less than 50 kpc. In those three cases (J1241, J1555, J2253 z_{gal} =0.1537), the O VI resides to one side of the galaxy systemic velocity so it is possible that those exhibit signatures of gas outflows.

The middle panel shows the rotational angular velocity, v_θ, where positive velocities indicate gas is rotating in the same direction as the galaxy. The major axis gas is rotating in the same direction as the galaxy as it infalls towards the disk. The rotation velocity component increase within 100 kpc and becomes the dominant velocity component near the galaxy. Thus, we should see clear signatures of co-rotation in our observations. The minor axis gas may be rotating in a similar direction within 25 kpc, but then scatters around zero, showing little sign of following the direction of galaxy rotation.

The last panel shows the polar velocity which is the rate of change of the angle between the vector to the cell and the z-axis, which is aligned with the galaxy's angular momentum vector. This is the lowest velocity component for the major axis gas, showing that this gas is primarily infalling, co-rotating and not mixing very much azimuthally. The minor axis gas has roughly zero polar velocity within 50 kpc and beyond 125 kpc. Between 50 and 125 kpc, the gas begins to have negative velocities. This occurs over the same impact parameter range where the radial velocity of the minor axis gas transitions from outflowing accelerating velocities to decelerating and accreting velocities, indicating a change in the behavior of the kinematics of minor axis O VI gas. This is a signature of the O VI returning back to the disk-plane of the galaxy. Overall the dominant minor axis velocity component is radial, be it outflowing or accreting.

5. DISCUSSION

The amount of O VI surrounding galaxies is significant and we are just beginning to understand the role of O VI in the CGM and its origins.

Nielsen et al. (2017) attempted to address the origins of the O VI absorption by examining their kinematic profiles. The O VI absorption velocity spread is more extended than for Mg II absorption, suggesting the two ions trace different parts of the CGM. Furthermore, in contrast to Mg II that shows different kinematics as a function of galaxy color, inclination and azimuthal angle, O VI is kinematically homogeneous regardless of galaxy property. This is consistent with our results where, unlike Mg II, we do not find any clear kinematic signature of co-rotation/accretion or signatures of definitive outflowing gas relative to the host galaxy. O VI found along the major axis of galaxies tends to span the entire rotation curve of their host galaxy, with the average O VI major axis spectra centered at the galaxy systemic velocity (only offset by 2.5 km s^{-1}) and spans from roughly $\pm$200 km s^{-1}. Only one of the O VI major axis systems could be explained by a co-rotation model. Overall, roughly 50% of the O VI optical depth can be found to either side of the galaxy rotation curve with no preference for rotation direction. It is still plausible that some of the O VI could be rotating in the same direction as the galaxy, we just have no way of differentiating that component relative to the rest of the O VI.

We further find that the O VI along the minor axis of galaxies does not show clear signs of co-rotation, with only three of ten systems that have relative galaxy and gas kinematics that can be modeled well with a co-rotation model. The remainder of the systems have the bulk of the gas counter-rotating with respect to the galaxy. Maybe this is not so surprising given that the gas is not located in the plane of the disk, but off-axis co-rotation is still common for Mg II absorbers (e.g., Kacprzak et al. 2010).

We further apply simple outflow models in an attempt to constrain the probability of outflows driving the observed O VI kinematics. Interestingly, we find that accelerating outflows can only occur when opening angles are small. The remainder of the parameter space has the O VI decelerating and falling back on the galaxy. This could be why in the stacked minor

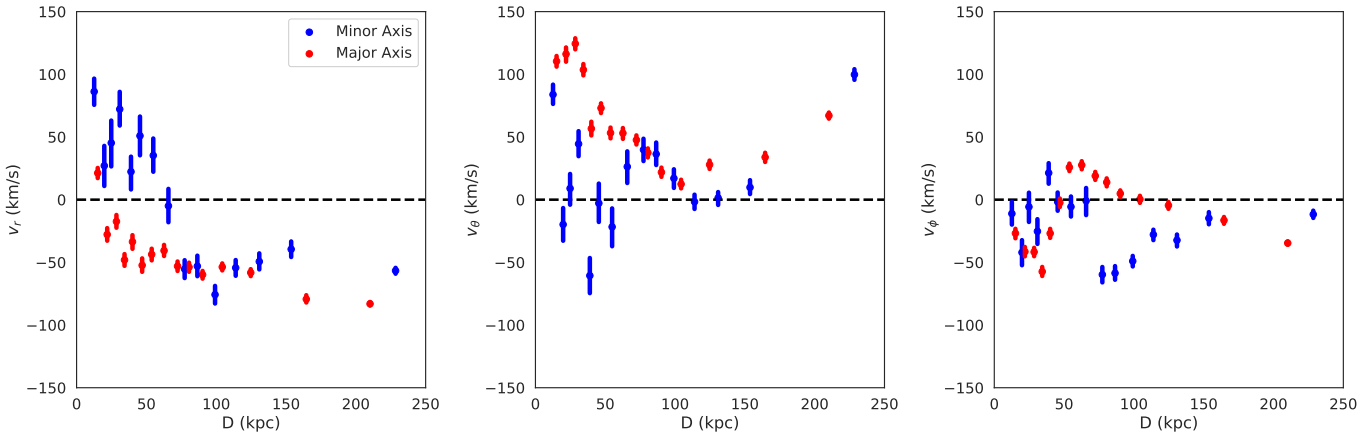

FIG. 10.— Median O VI velocities averaged over the eight simulations shown for the major axis and minor axis. Major axis gas is defined as having an azimuthal angle less than 30 degrees while minor axis gas has an azimuthal angle greater than 40 degrees. The first panel shows the radial velocity for major and minor axis gas in red and blue respectively along with the standard error in the mean. The middle panel shows the rotational angular velocity where positive velocities indicate O VI gas rotating in the same direction of the galaxy. The last panel shows the polar velocity, which is the rate of change of the angle between the vector to the cell and the z-axis, which is aligned with the galaxy's angular momentum vector.

axis O VI profiles only have a systematic offset of 28 km s^{-1} from the galaxy systemic velocity. Again, this would be kinematically different compared to what is seen for Mg II where, over a similar impact parameter range, Mg II gas tends to have accelerated flows (Bouché et al. 2012; Bordoloi et al. 2014; Schroetter et al. 2016). However, these observed O VI kinematics are consistent with simulations having predicted that a possible origin of O VI is from ancient outflows, which would eventually fall back to the galaxy (e.g., Ford et al. 2014, 2016; Oppenheimer et al. 2016). So it is possible that we are seeing the kinematic signatures of the gas recycling from ancient outflows.

Our simulations show that O VI can be found in filamentary structures and within outflow winds as seen in Figure 7. The O VI has a radial velocity flow towards the galaxy starting at −80 km s^{-1} at 200 kpc and reduces in speed as it approaches the galaxy along with major axis (see Figure 10). This the rotational speed of the infalling gas also increases as it approaches the galaxy and shows little sign of azimuthal mixing as indicated by the low polar velocities. We find that minor axis O VI outflows of a modest velocity 50 km s^{-1} occur within the first 50 kpc, then decelerate and begin to fall back onto the galaxy (as indicated by the −50 km s^{-1} polar velocities). These gas flows appear quite obvious within the simulations, but the simulations contain a wealth of information and 1000s of lines-of-sight, so we typically show velocity medians and median column densities, but this is not how we observe O VI in reality. What we normally observe is integrated velocities and optical depths, which are quite different to median values.

In Figure 11, we show the histograms of the radial, rotational and polar velocities from the eight simulations. We define two sets of data. In the top panel, we select O VI gas cells within a cone of a half-opening angle 30 degrees around the major axis and 40 degrees half-opening angle around minor axis, over all impact parameters and show the velocity histogram of gas. Both major and minor axis gas peak at negative radial velocities since major axis gas is flowing along filaments and the minor axis gas in falling back to the galaxy, with some additional power at positive velocities for the minor axis outflowing gas. For rotational velocity the major axis gas peaks at positive velocities since it is rotating in the same direction of the galaxy, while minor axis gas has a bimodal distribution exhibiting both co- and counter-rotating velocities. The major axis gas also exhibits a peak at systemic polar velocity while minor axis gas peaks at negative velocities indicating gas can be accreting back onto the galaxy.

In the bottom panel of Figure 11, we show a histogram of velocities for all the O VI gas cells along the quasar sightlines through the entire galaxy halo. Note that significant kinematic features become lost and major and minor axis gas have a similar velocity structure, which is what we see in our observations shown in Figure 9. The stronger radial outflow component becomes lost along with the co- and counter-rotating gas. Both major and minor axis gas have similar distributions in all velocity components. This implies that gas all along the quasar sightlines through the entire halo conspires to line up in velocity, masking any signatures of gas flows. So although it is likely that there is some fraction of the observed O VI that could be tracing accretion and outflows, we are unable to quantify this with our observations.

Although Kacprzak et al. (2015) reported that the spatial O VI azimuthal dependence is a result of gas major axis-fed inflows/recycled gas and minor axis-driven outflows, it is impossible to confirm this using the kinematics of O VI alone. Furthermore, Nielsen et al. (2017) postulated that the higher column densities found near the major and minor axes of galaxies, as traced by Mg II absorption, my provide a shield such that O VI is not so easily further ionized as it would be at intermediate azimuthal angles. This would naturally produce an azimuthal dependence without O VI being directly linked to outflows and accretion. Disentangling these two ideas will require much more investigation using multi-phase gas tracers.

Overall, although the simulations indicate that O VI is present in inflowing and outflowing gas, observationally it seems that O VI is not ideal to use as a kinematic tracer of gas flows within the galaxy. It might be further complicated by the fact that the simulations predict collisional ionized O VI is dominant in the central regions of halos (inside $0.2-0.3$ R_{vir}), while photoionization is more significant at the outskirts around R_{vir} (Roca-Fàbrega et al. 2018). It is likely that O VI is more indicative of the thermal motions of

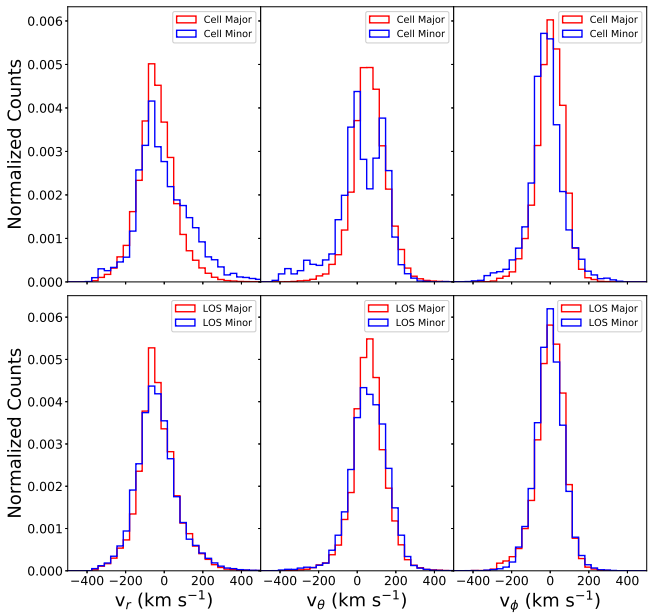

FIG. 11.— Histograms of the radial and rotational velocities from the eight simulations. (Top) We select gas cells within a cone of an opening angle ±30 degrees around the major axis and ±50 degrees around the minor axes showing the velocity histogram of gas that is likely infalling and outflowing. We choose these regions in order to select gas likely only associated with gas flows. (Bottom) Histogram of the velocities for all the gas cells along the quasar sightlines through the entire halo, selecting all gas though the halo showing the full range of velocities being intercepted. Note that significant kinematic features become lost and that there is a lot of gas at similar velocities both align along the major and minor axis.

the gas probing the temperature of the dark matter halos (Oppenheimer et al. 2016; Roca-Fàbrega et al. 2018) though this remains highly debated. A halo mass dependence has been directly observed for O VI (Ng et al. 2019; Pointon et al. 2017) leading credence to the thermal temperature model.

6. CONCLUSIONS

We have constructed a sub-sample from Kacprzak et al. (2015) of 20 O VI absorption systems (EW>0.1 Å) associated with isolated galaxies that have accurate spectroscopic redshifts and rotation curves obtained from Keck/ESI. Given the observed O VI azimuthal angle bimodality (Kacprzak et al. 2015), our sample is split into two azimuthal angle bins described as major axis ($\Phi < 25$ degrees) and minor axis ($\Phi > 33$ degrees) samples. Our results are summarized as follows:

1. The O VI absorption found along the major axis (within Φ = 25 degrees) of their host galaxy does not show any significant correlation with galaxy rotation and O VI kinematics. Only one system can be explained by simple rotation/accretion model. This is in contrast to co-rotation commonly observed for Mg II absorption systems. The O VI absorption kinematics span the entire dynamical range of their host galaxies and have a relative velocity offset of only 2.5 km s^{-1} from the galaxy systemic velocity.

2. The O VI found along the minor axis of galaxies ($\Phi >$ 33 degrees) could be modeled by outflows. Simple models show that only over a small parameter space (with small opening angles) O VI can be accelerating in outflows. The rest of the time the gas must be decelerating and being recycled, which is consistent with simulations. The absorption redshift has a velocity offset of 28.0 km s^{-1} relative to the host galaxy systemic velocity.

3. 3-D visualization of our simulations shows that O VI is contained in filaments and in a spherical halo of ∼50 kpc in size surrounding the host galaxy. This implies that we should see kinematic signatures of O VI within the simulations.

4. The O VI absorption-lines created from sightlines passing through the simulations along the major and minor axes have similar optical depths, velocity widths and have differ only in a kinematic shape. This difference is likely attributed to differences in galaxy properties such as inclination.

5. All O VI identified in the simulated sightlines along the major axis have kinematics consistent with gas accretion along filaments, which decelerate as they approach the host galaxy. Infalling gas also rotates in the same direction of the galaxy, and increases in velocity as it approaches the galaxy. Thus O VI can trace gas accretion.

6. All O VI identified in the simulated sightlines along the minor show that outflows only have positive velocities within the inner 50-75 kpc where they eventually decelerate and fall back in towards at around −50 km s^{-1}.

7. The kinematic signatures in the simulations are quite clear when computing median velocities and column densities. However, when we compare these to apparent kinematic signatures integrated along lines of sight, we find that strong gas kinematic signatures are washed out due to existing velocity structure from all the different structures through the halo and the diffuse gas between them.

Although we do not know the true origins of O VI, it appears to not serve as a useful kinematic indicator of ongoing gas accretion, outflows or star-formation. Ions such as Mg II, Si II and Ca II have all indicated that they are better tracers of gas kinematics even over the same H I column density range as O VI. Ng et al. (2019) and Pointon et al. (2017) show clear evidence that O VI is halo mass dependent, efficiently probing the viral temperature of the halo as predicted in the simulations (Oppenheimer et al. 2016; Roca-Fàbrega et al. 2018). Although O VI can trace interesting phenomena within galaxy halos, this is masked by all the diffuse gas found ubiquitously within the halos at velocities of ∼±200 km s^{-1}. The interest in O VI has increased in recent years due to the ease it can be simulated in cosmological simulations, and from *HST*/COS initiatives, but we must now turn more of our efforts to simulating the cool CGM in order to place reasonable gas physics constraints on galaxy growth and evolution.

We thank Roberto Avila (STScI) for his help and advice with modeling PSFs with ACS and WFC3. GGK acknowledges the support of the Australian Research Council through the award of a Future Fellowship (FT140100933). GGK and NMN acknowledges the support of the Australian Research

Council through a Discovery Project DP170103470. CWC and JCC are supported by NASA through grants HST GO-13398 from the Space Telescope Science Institute, which is operated by the Association of Universities for Research in Astronomy, Inc., under NASA contract NAS5-26555. CWC and JCC are further supported by NSF AST-1517816. SM acknowledges support from the ERC grant 278594-GasAroundGalaxies. DC been funded by the ERC Advanced Grant, STARLIGHT: Formation of the First Stars (project number 339177). The VELA simulations were performed at the National Energy Research Scientific Computing Center (NERSC) at Lawrence Berkeley National Laboratory, and at NASA Advanced Supercomputing (NAS) at NASA Ames Research Center. Most of the data presented here were obtained at the W. M. Keck Observatory, which is operated as a scientific partnership among the California Institute of Technology, the University of California, and the National Aeronautics and Space Administration. The Observatory was made possible by the generous financial support of the W. M. Keck Foundation. Observations were supported by Swinburne Keck programs 2016A_W056E, 2015B_W018E, 2014A_W178E and 2014B_W018E. The authors wish to recognize and acknowledge the very significant cultural role and reverence that the summit of Mauna Kea has always had within the indigenous Hawaiian community. We are most fortunate to have the opportunity to conduct observations from this mountain. Based on observations made with the NASA/ESA Hubble Space Telescope, and obtained from the Hubble Legacy Archive, which is a collaboration between the Space Telescope Science Institute (STScI/NASA), the Space Telescope European Coordinating Facility (ST-ECF/ESA) and the Canadian Astronomy Data Centre (CADC/NRC/CSA).

Facilities: Keck II (ESI) HST (COS, WFPC2, ACS, WFC3).

REFERENCES

Asplund, M., Grevesse, N., Sauval, A. J., & Scott, P. 2009, ARA&A, 47, 481
Barro, G., Faber, S. M., Pérez-González, P. G., et al. 2013, ApJ, 765, 104
Barro, G., Faber, S. M., Pérez-González, P. G., et al. 2014, ApJ, 791, 52
Bertin, E., & Arnouts, S. 1996, A&AS, 117, 393
Bergeron, J., & Boissé, P. 1991, A&A, 243, 334
Bordoloi, R., Lilly, S. J., Kacprzak, G. G., & Churchill, C. W. 2014, ApJ, 784, 108
Bordoloi, R., Lilly, S. J., Knobel, C., et al. 2011, ApJ, 743, 10
Bouché, N., Hohensee, W., Vargas, R., Kacprzak, G. G., et al. 2012, MNRAS, 426, 801
Bouché, N., Murphy, M. T., Kacprzak, G. G., et al. 2013, Science, 341, 50
Bouché, N., Murphy, M. T., Péroux, C., Csabai, I. & Wild. V. 2006 MNRAS, 371, 495
Carswell, R. F., & Webb, J. K. 2014, Astrophysics Source Code Library, ascl:1408.015
Ceverino, D., Arribas, S., Colina, L., et al. 2016, MNRAS, 460, 2731
Ceverino, D., Dekel, A., & Bournaud, F. 2010, MNRAS, 404, 2151
Ceverino, D., & Klypin, A. 2009, ApJ, 695, 292
Ceverino, D., Klypin, A., Klimek, E. S., et al. 2014, MNRAS, 442, 1545
Chelouche, D., & Bowen, D. V. 2010, ApJ, 722, 1821
Chen, H.-W., Helsby, J. E., Gauthier, J.-R., Shectman, S. A., Thompson, I. B., & Tinker, J. L. 2010a, ApJ, 714, 1521
Chen, H.-W., & Mulchaey, J. S. 2009, ApJ, 701, 1219
Chen, H.-W., Lanzetta, K. M., Webb, J. K., & Barcons, X. 2001, ApJ, 559, 654
Churchill, C. W., Kacprzak, G. G., Steidel, C. C., et al. 2012, ApJ, 760, 68
Churchill, C. W., Klimek, E., Medina, A., & Vander Vliet, J. R. 2014, arXiv:1409.0916
Churchill, C. W., Mellon, R. R., Charlton, J. C., Jannuzi, B. T., Kirhakos, S., Steidel, C. C., & Schneider, D. P. 2000a, ApJS, 130, 91
Churchill, C. W., Nielsen, N. M., Kacprzak, G. G., & Trujillo-Gomez, S. 2013, ApJ, 763, L42
Churchill, C. W., Trujillo-Gomez, S., Nielsen, N. M., & Kacprzak, G. G. 2013, ApJ, 779, 87
Churchill, C. W., Vander Vliet, J. R., Trujillo-Gomez, S., Kacprzak, G. G., & Klypin, A. 2015, ApJ, 802, 10
Churchill, C. W., & Vogt, S. S. 2001, AJ, 122, 679
Coil, A. L., Weiner, B. J., Holz, D. E., et al. 2011, ApJ, 743, 46
Crighton, N. H. M., Hennawi, J. F., Simcoe, R. A., et al. 2015, MNRAS, 446, 18
Danovich, M., Dekel, A., Hahn, O., Ceverino, D., & Primack, J. 2015, MNRAS, 449, 2087
Danforth, C. W., Stocke, J. T., & Shull, J. M. 2010, ApJ, 710, 613
Dekel, A., & Birnboim, Y. 2006, MNRAS, 368, 2
Draine, B. T. 2011, Physics of the Interstellar and Intergalactic Medium, Princeton University Press, ISBN: 978-0-691-12214-4 (Table 1.4, p8)
Ford, A. B., Werk, J. K., Davé, R., et al. 2016, MNRAS, 459, 1745
Ford, A. B., Davé, R., Oppenheimer, B. D., et al. 2014, MNRAS, 444, 1260
Fox, A. J., Lehner, N., Tumlinson, J., et al. 2013, ApJ, 778, 187
Fox, A. J., Prochaska, J. X., Ledoux, C., et al. 2009, A&A, 503, 731
Gauthier, J.-R., & Chen, H.-W. 2012, MNRAS, 424, 1952
Gonzaga, S., Hack, W., Fruchter, A., Mack, J., eds. 2012, The DrizzlePac Handbook. (Baltimore, STScI)
Guillemin p., & Bergeron, J. 1997, A&A, 328, 499
Gutcke, T. A., Stinson, G. S., Macciò, A. V., Wang, L., & Dutton, A. A. 2017, MNRAS, 464, 2796
Haardt, F., & Madau, P. 2012, ApJ, 746, 125
Ho, S. H., Martin, C. L., Kacprzak, G. G., & Churchill, C. W. 2017, ApJ, 835, 267
Hummels, C. B., Bryan, G. L., Smith, B. D., & Turk, M. J. 2013, MNRAS, 430, 1548
Johnson, S. D., Chen, H.-W., & Mulchaey, J. S. 2015, MNRAS, 449, 3263
Kacprzak, G. G. 2017, Gas Accretion onto Galaxies, 430, 145
Kacprzak, G. G., Cooke, J., Churchill, C. W., Ryan-Weber, E. V., & Nielsen, N. M. 2013, ApJ, 777, L11
Kacprzak, G. G., Churchill, C. W., Barton, E. J., & Cooke, J. 2011a, ApJ, 733, 105
Kacprzak, G. G., Churchill, C. W., Ceverino, D., Steidel, C. C., Klypin, A., & Murphy, M. T. 2010, ApJ, 711, 533
Kacprzak, G. G., Churchill, C. W., Evans, J. L., Murphy, M. T., & Steidel, C. C. 2011b, MNRAS, 416, 3118
Kacprzak, G. G., Churchill, C. W., Steidel, C. C., & Murphy, M. T. 2008, AJ, 135, 922
Kacprzak, G. G., Churchill, C. W., & Nielsen, N. M. 2012, ApJ, 760, L7
Kacprzak, G. G., Churchill, C. W., Steidel, C. C., Spitler, L. R., & Holtzman, J. A. 2012, MNRAS, 427, 3029
Kacprzak, G. G., Martin, C. L., Bouché, N., et al. 2014, ApJ, 792, L12
Kacprzak, G. G., Muzahid, S., Churchill, C. W., Nielsen, N. M., & Charlton, J. C. 2015, ApJ, 815, 22
Kereš, D., Katz, N., Weinberg, D. H., & Davé, R. 2005, MNRAS, 363, 2
Klypin, A., Kravtsov, A. V., Bullock, J. S., & Primack, J. R. 2001, ApJ, 554, 903
Klypin, A. A., Trujillo-Gomez, S., & Primack, J. 2011, ApJ, 740, 102
Kravtsov, A. V. 1999, Ph.D. Thesis
Kravtsov, A. V. 2003, ApJ, 590, L1
Kriss, G. A. 2011, COS Instrument Science Report 2011-01(v1), 17 pages, 1
Krogager, J.-K., Fynbo, J. P. U., Ledoux, C., et al. 2013, MNRAS, 433, 3091
Lan, T.-W., Ménard, B., & Zhu, G. 2014, ApJ, 795, 31
Lan, T.-W., & Mo, H. 2018, arXiv:1806.05786
Liang, C. J., Kravtsov, A. V., & Agertz, O. 2016, MNRAS, 458, 1164
Lopez, S., Tejos, N., Ledoux, C., et al. 2018, Nature, 554, 493
Maller, A. H., & Bullock, J. S. 2004, MNRAS, 355, 694
Mathes, N. L., Churchill, C. W., Kacprzak, G. G., et al. 2014, ApJ, 792, 128
Martin, C. L., & Bouché, N. 2009, ApJ, 703, 1394
Martin, C. L., Shapley, A. E., Coil, A. L., et al. 2012, ApJ, 760, 127
Ménard, B., & Fukugita, M. 2012, ApJ, 754, 116
Meiring, J. D., Tripp, T. M., Werk, J. K., et al. 2013, ApJ, 767, 49
Mo, H. J., & Miralda-Escude, J. 1996, ApJ, 469, 589
Muzahid, S., Kacprzak, G. G., Churchill, C. W., et al. 2015, ApJ, 811, 132
Narayanan, A., Savage, B. D., Mishra, P. K., et al. 2018, MNRAS, 475, 3529
Narayanan, A., Savage, B. D., & Wakker, B. P. 2012, ApJ, 752, 65
Nelson, D., Kauffmann, G., Pillepich, A., et al. 2018, MNRAS, 477, 450
Ng, M., Nielsen, N. M., Kacprzak, G. G., et al. 2019, submitted
Nielsen, N. M., Churchill, C. W., Kacprzak, G. G., & Murphy, M. T. 2013, ApJ, 776, 114
Nielsen, N. M., Churchill, C. W., Kacprzak, G. G., Murphy, M. T., & Evans, J. L. 2016, ApJ, 818, 171
Nielsen, N. M., Churchill, C. W., Kacprzak, G. G., Murphy, M. T., & Evans, J. L. 2015, ApJ, 812, 83
Nielsen, N. M., Kacprzak, G. G., Muzahid, S., et al. 2017, ApJ, 834, 148
Nestor, D. B., Johnson, B. D., Wild, V., et al. 2011, MNRAS, 412, 1559
Noterdaeme, P., Laursen, P., Petitjean, P., et al. 2012, A&A, 540, A63
Noterdaeme, P., Srianand, R., & Mohan, V. 2010, MNRAS, 403, 906
Oppenheimer, B. D., Crain, R. A., Schaye, J., et al. 2016, MNRAS, 460, 2157
Oppenheimer, B. D., Segers, M., Schaye, J., Richings, A. J., & Crain, R. A. 2018, MNRAS, 474, 4740
Pachat, S., Narayanan, A., Muzahid, S., et al. 2016, MNRAS, 458, 733
Peeples, M. S., Werk, J. K., Tumlinson, J., et al. 2014, ApJ, 786, 54
Péroux, C., Bouché, N., Kulkarni, V. P., & York, D. G. 2013, MNRAS, 436, 2650
Pointon, S. K., Nielsen, N. M., Kacprzak, G. G., et al. 2017, ApJ, 844, 23

Prochaska, J. X., Weiner, B., Chen, H.-W., Mulchaey, J., & Cooksey, K. 2011, ApJ, 740, 91
Roca-Fàbrega, S., Dekel, A., Faerman, Y., et al. 2018, arXiv:1808.09973
Rosenwasser, B., Muzahid, S., Charlton, J. C., et al. 2018, MNRAS, 476, 2258
Rubin, K. H. R., Diamond-Stanic, A. M., Coil, A. L., Crighton, N. H. M., & Moustakas, J. 2018, ApJ, 853, 95
Rubin, K. H. R., Prochaska, J. X., Koo, D. C., et al. 2014, ApJ, 794, 156
Rubin, K. H. R., Prochaska, J. X., Koo, D. C., Phillips, A. C., & Weiner, B. J. 2010, ApJ, 712, 574
Savage, B. D., Lehner, N., & Narayanan, A. 2011, ApJ, 743, 180
Schroetter, I., Bouché, N., Wendt, M., et al. 2016, ApJ, 833, 39
Sérsic, J. L. 1968, Cordoba, Argentina: Observatorio Astronomico
Sheinis, A. I., Bolte, M., Epps, H. W., Kibrick, R. I., Miller, J. S., Radovan, M. V., Bigelow, B. C., & Sutin, B. M. 2002, PASP. 114, 851
Simard, L., Willmer, C. N. A., Vogt, N. P., Sarajedini, V. L., Philips, A. C., Weiner, B. J., Koo, D. C., Im, M., Illingworth, G. D., & Faber, S. M. 2002, ApJS, 142, 1
Steidel, C. C. 1995, in QSO Absorption Lines, ed. G. Meylan, (Springer–verlag: Berlin Heidelberg), p. 139
Steidel, C. C., Kollmeier, J. A., Shapely, A. E., Churchill, C. W., Dickinson, M., & Pettini, M. 2002, ApJ, 570, 526
Stewart, K. R., Brooks, A. M., Bullock, J. S., et al. 2013, ApJ, 769, 74
Stewart, K. R., Kaufmann, T., Bullock, J. S., et al. 2011, ApJ, 738, 39
Stewart, K. R., Maller, A. H., Oñorbe, J., et al. 2017, ApJ, 843, 47
Stocke, J. T., Keeney, B. A., Danforth, C. W., et al. 2013, ApJ, 763, 148
Stocke, J. T., Penton, S. V., Danforth, C. W., et al. 2006, ApJ, 641, 217
Suresh, J., Rubin, K. H. R., Kannan, R., et al. 2017, MNRAS, 465, 2966
Tremonti, C. A., Moustakas, J., & Diamond-Stanic, A. M. 2007, ApJl, 663, L77
Tripp, T. M., Jenkins, E. B., Bowen, D. V., et al. 2005, ApJ, 619, 714
Tripp, T. M., Meiring, J. D., Prochaska, J. X., et al. 2011, Science, 334, 952
Tripp, T. M., Sembach, K. R., Bowen, D. V., et al. 2008, ApJS, 177, 39
Trujillo-Gomez, S., Klypin, A., Primack, J., & Romanowsky, A. J. 2011, ApJ, 742, 16
Tumlinson, J., Shull, J. M., Giroux, M. L., & Stocke, J. T. 2005, ApJ, 620, 95
Tumlinson, J., Thom, C., Werk, J. K., et al. 2011, Science, 334, 948
Vander Vliet, Jacob R. 2017, Ph.D. Thesis,
van Dokkum, P. G. 2001, PASP, 113, 1420
Vogt, N. P., Forbes, D. A., Phillips, A. C., Gronwall, C., Faber, S. M., Illingworth, G. D., & Koo, D. C. 1996, ApJL, 465, L15
Wakker, B. P., & Savage, B. D. 2009, ApJS, 182, 378
Wakker, B. P., Savage, B. D., Fox, A. J., Benjamin, R. A., & Shapiro, P. R. 2012, ApJ, 749, 157
Walter, F., Weiss, A., & Scoville, N. 2002, ApJ, 580, L21
Weiner, B. J., et al. 2009, ApJ, 692, 187
Werk, J. K., Prochaska, J. X., Cantalupo, S., et al. 2016, ApJ, 833, 54
Werk, J. K., Prochaska, J. X., Thom, C., et al. 2012, ApJS, 198, 3
Werk, J. K., Prochaska, J. X., Tumlinson, J., et al. 2014, ApJ, 792, 8
Zolotov, A., Dekel, A., Mandelker, N., et al. 2015, MNRAS, 450, 2327

APPENDIX

A. MAJOR AXIS SAMPLE

Here we show 10 systems where the O VI absorption is detected with 25 degrees of the galaxy major axis. We present the data used in this analysis, which lncludes *HST*/COS O VI absorption spectra, *HST* imaging of the quasar and galaxy field, along with the Keck/ESI spectra for each galaxy to derive their rotation curves. We further present a simple rotating disk model as described in Section 3.2.

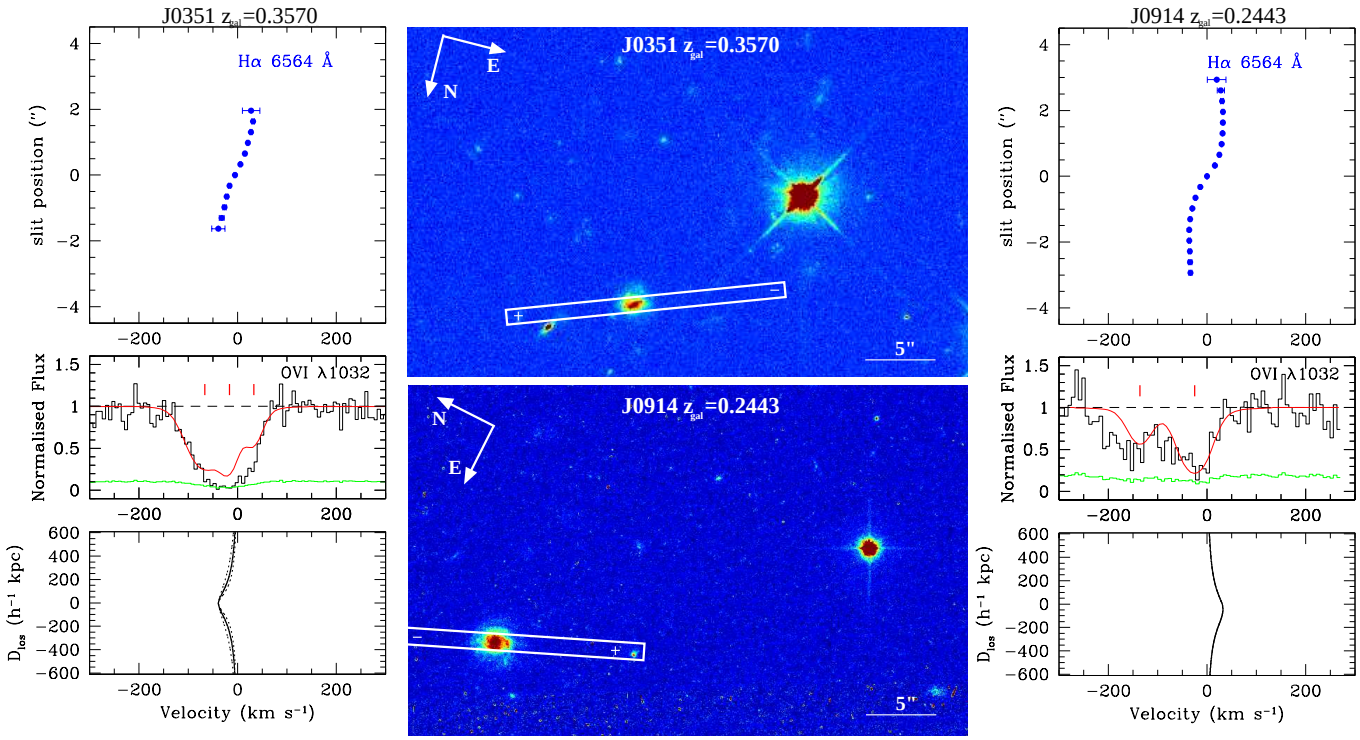

FIG. A1.— Same as Figure 2 – *HST* images and galaxy rotation curves presented for two fields where the quasar sight-line aligns with the galaxy's major axis. (Top middle) A $45'' \times 25''$ *HST* image of the quasar field J0351. The ESI/Keck slit is superimposed on the image over the targeted galaxy. The "+" and "−" on the slit indicate slit direction in positive and negative arcseconds where $0''$ is defined at the galaxy center. (Left) The $z = 0.3570$ galaxy rotation curve and the *HST*/COS O VI λ1031 absorption profile is shown with respect to the galaxy systemic velocity. The panel below the O VI absorption is a simple disk rotation model computed using Equation 1, which is a function of the galaxy rotation speed and orientation with respect to the quasar sight-line. The J0351 galaxy is rotating in the same direction as the absorption however, the velocity range covered by the model is not consistent with the entire range covered by the absorption profile. (Bottom middle) Same as top middle except for the J0914 quasar field and for the targeted galaxy at $z = 0.2443$ (Right) Same as left except the $z = 0.2443$ in the J0914 quasar field. Note here that the O VI absorption is consistent with being counter-rotating with respect to the galaxy and again, the model has insufficient velocities to account for all the absorption kinematics. In both cases disk-rotation does not reproduce the observed absorption velocities.

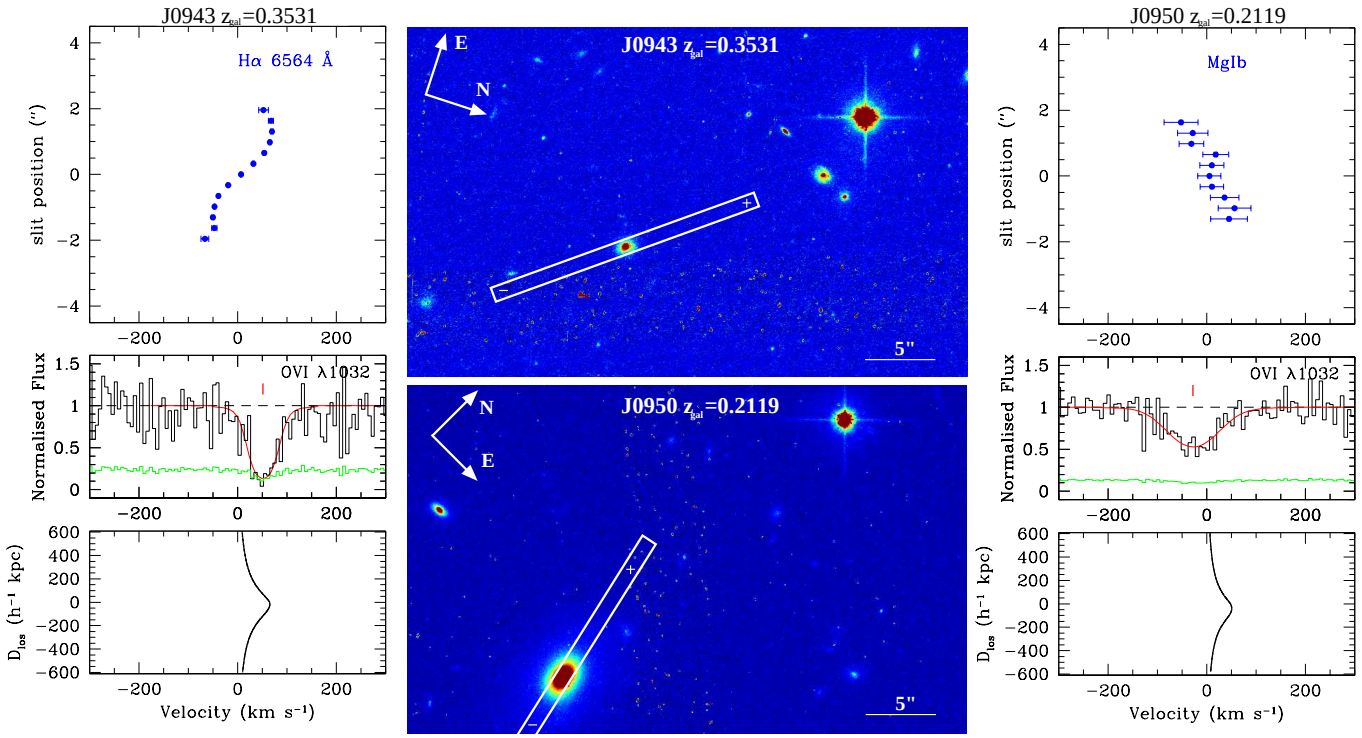

FIG. A2.— Same as Figure A1 except for top-middle and left is for the J0943 field with the $z = 0.3531$ galaxy and bottom-middle and right is for J0950 field with the $z = 0.2119$ galaxy. The J0943 $z = 0.3531$ galaxy has a rotation velocity that matches the observed O VI absorption kinematics. The J0950 $z = 0.2119$ galaxy is counter-rotating with respect to the bulk of the O VI absorption.

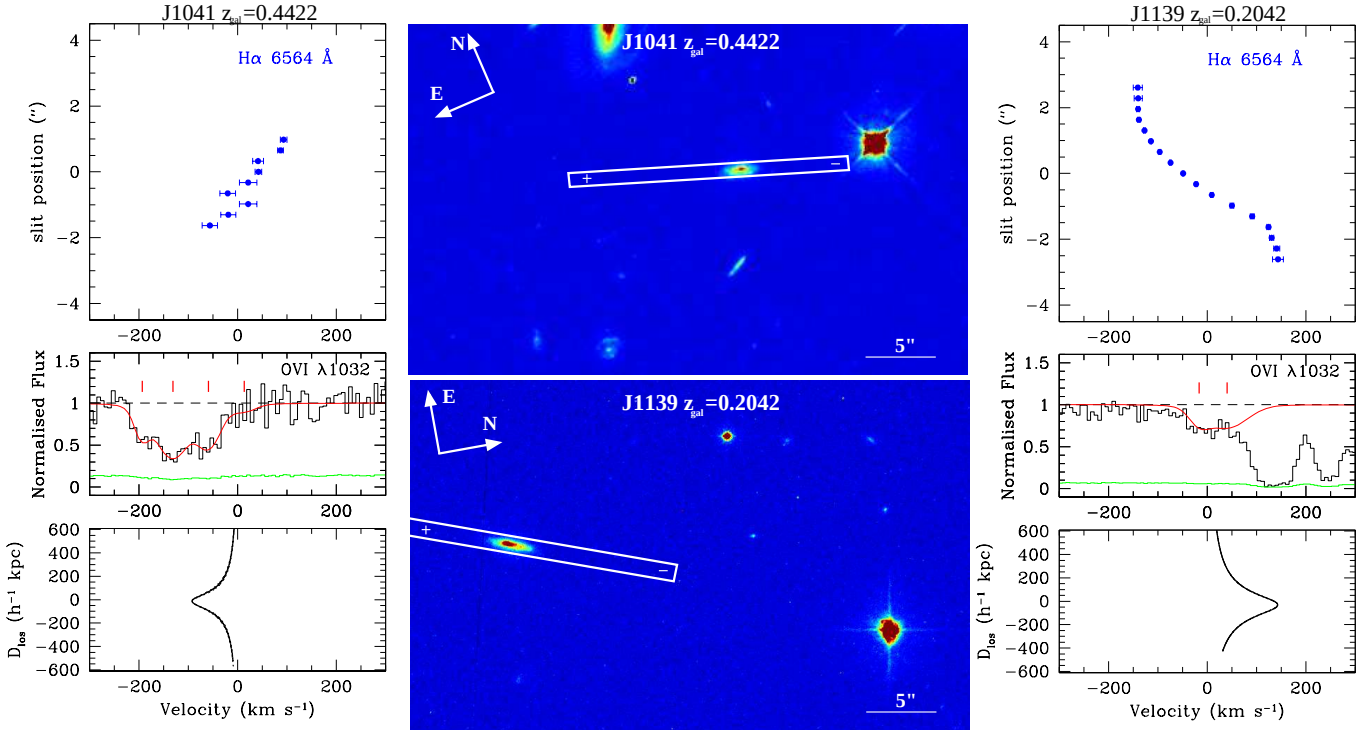

FIG. A3.— Same as Figure A1 except for top-middle and left is for the J1041 field with the $z = 0.4422$ galaxy and bottom-middle and right is for J1139 field with the $z = 0.2042$ galaxy. The J1041 $z = 0.4422$ galaxy has a rotation velocity that matches the observed O VI absorption kinematics. It slightly under-predicts the O VI absorption velocity, yet this could be due to the not covering the full rotation curve with our observations.The J1139 $z = 0.2042$ galaxy has a rotation velocity that matches the observed O VI absorption kinematics.

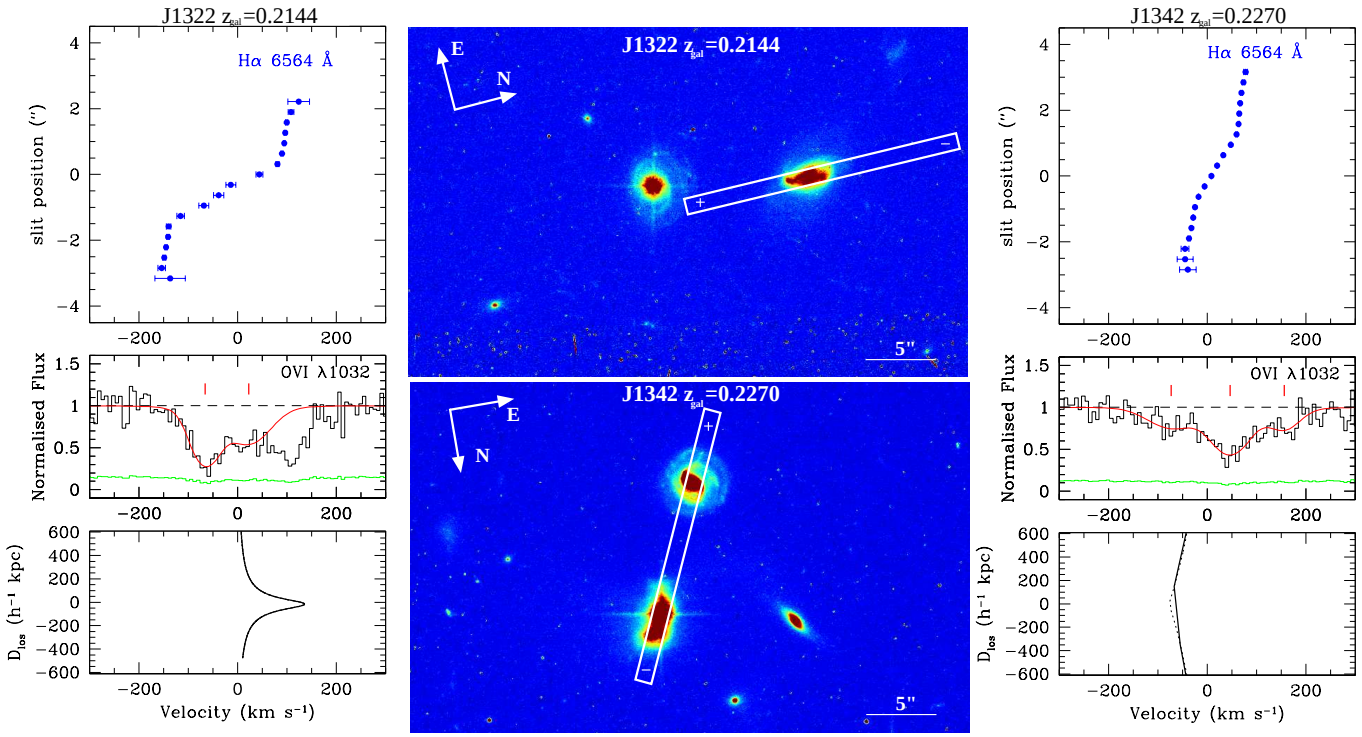

FIG. A4.— Same as Figure A1 except for top-middle and left is for the J1322 field with the $z = 0.2144$ galaxy and bottom-middle and right is for J1342 field with the $z = 0.2270$ galaxy. Both galaxies here are counter-rotating with respect to the bulk of the O VI absorption.

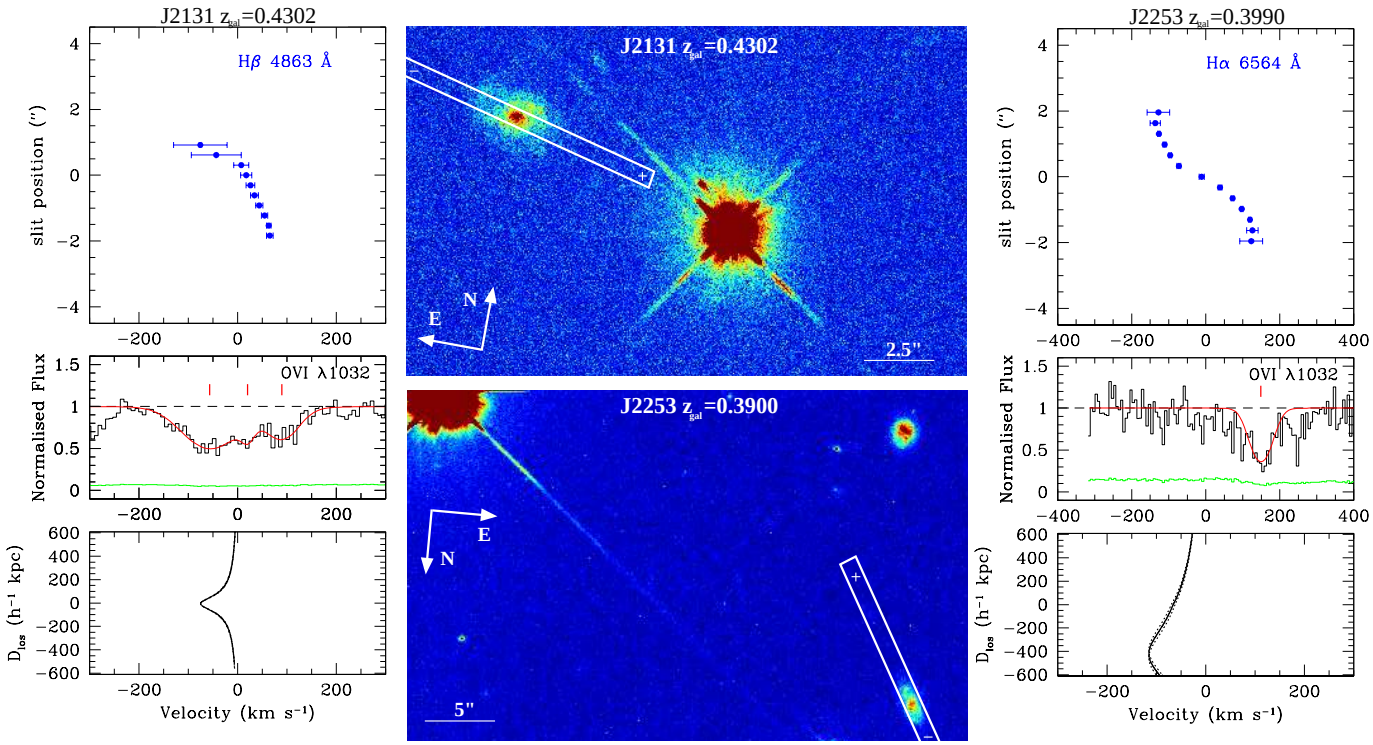

FIG. A5.— Same as Figure A1 except for top-middle and left is for the J2131 field with the $z = 0.4302$ galaxy and bottom-middle and right is for J2253 field with the $z = 0.3900$ galaxy. Both galaxies here are counter-rotating with respect to the bulk of the O VI absorption.

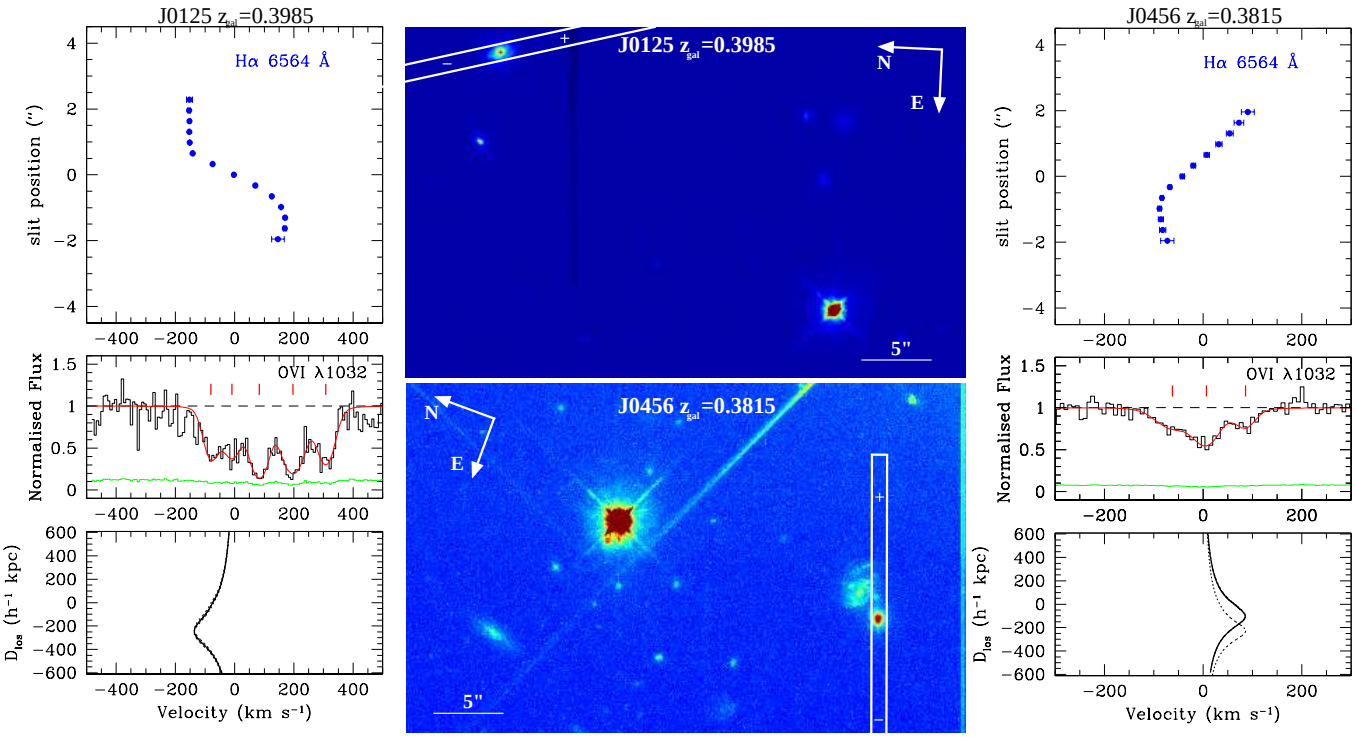

FIG. B1.— Same as Figure A1 except for top-middle and left is for the J1025 field with the $z = 0.3985$ galaxy and bottom-middle and right is for J0456 field with the $z = 0.3815$ galaxy. For the J1025 $z = 0.3985$ galaxy, the O VI has a large velocity spread that extends opposite to the rotational direction of the galaxy. The J0456 $z = 0.3815$ galaxy is counter-rotating with respect to the bulk of the O VI absorption.

B. MINOR AXIS SAMPLE

Here we show 10 systems where the O VI absorption is detected azimuthal angles of greater than 33 degrees as measured from the galaxy major axis. We again present the data used in this analysis, which Includes *HST*/COS O VI absorption spectra, *HST* imaging of the quasar and galaxy field, along with the Keck/ESI spectra for each galaxy to derive their rotation curves. Although this is a minor axis sample, we stil present the simple rotating disk model as described in Section 3.2.

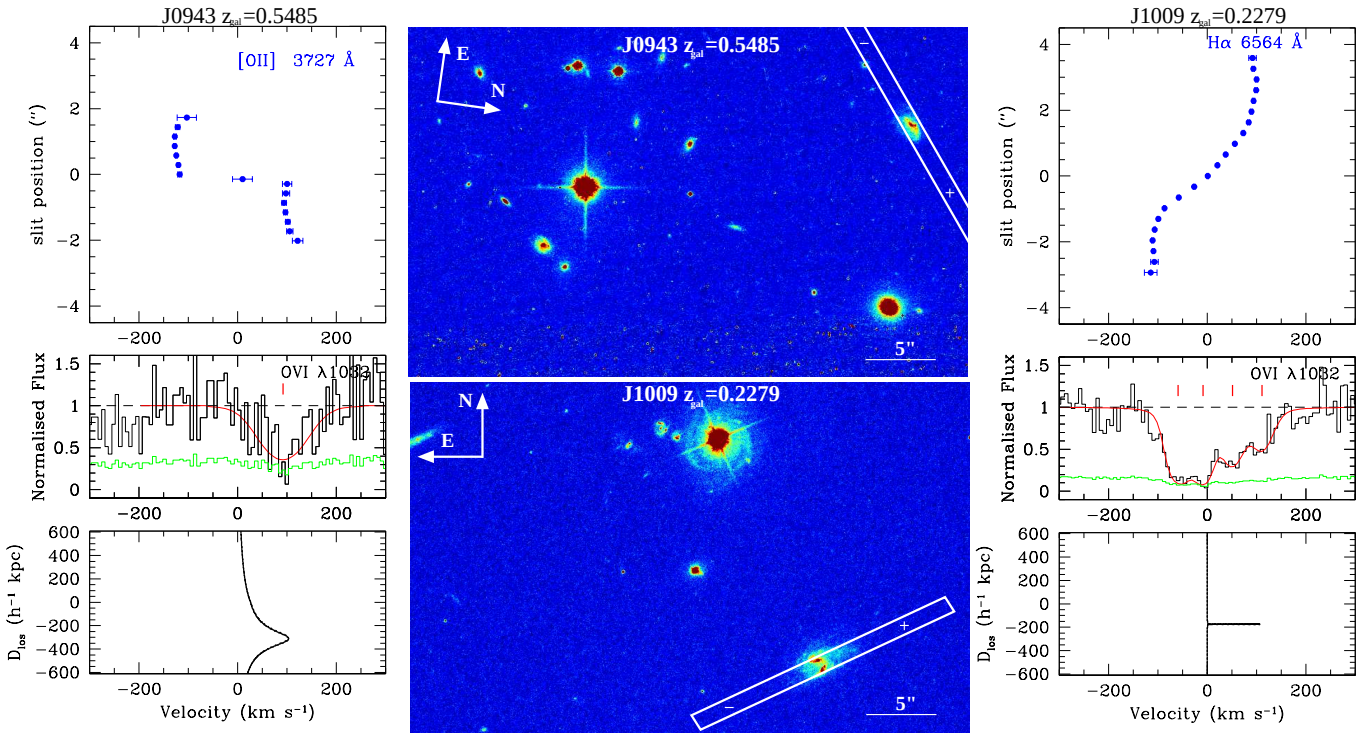

FIG. B2.— Same as Figure A1 except for top-middle and left is for the J0943 field with the $z = 0.5485$ galaxy and bottom-middle and right is for J1009 field with the $z = 0.2279$ galaxy. For the J0943 $z = 0.5485$ galaxy, the O VI has a large velocity spread that extends opposite to the rotational direction of the galaxy. The J1009 $z = 0.2279$ galaxy is counter-rotating with respect to the bulk of the O VI absorption.

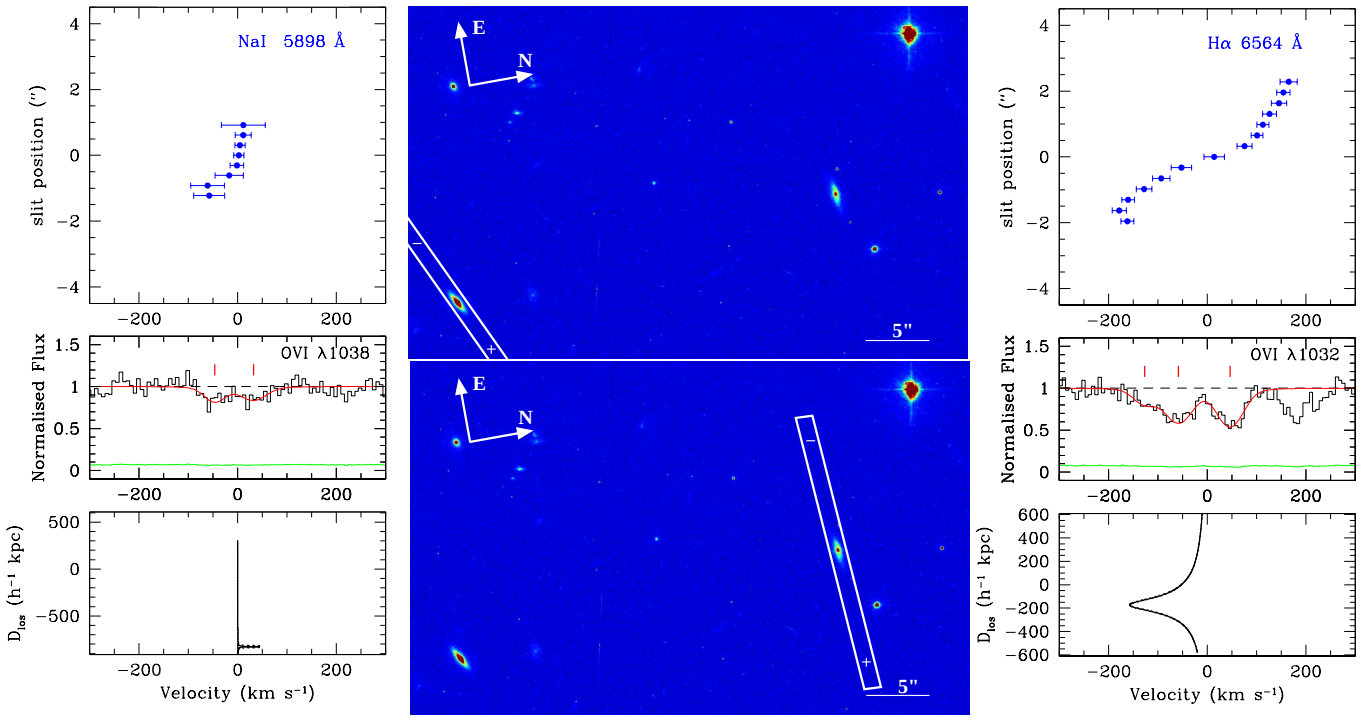

FIG. B3.— Same as Figure A1 except that a $55'' \times 35''$ *HST* in middle top and bottom panels is for the J1136 field. The left panel is shown for the $z = 0.2123$ galaxy and the right is shown $z = 0.3193$ galaxy. The O VI for both galaxies spans boths sides of the systemic velocity, with little-to-no absorption at the systemic velocity. In both cases, the galaxies are counter-rotating with respect to roughly half of the O VI absorption.

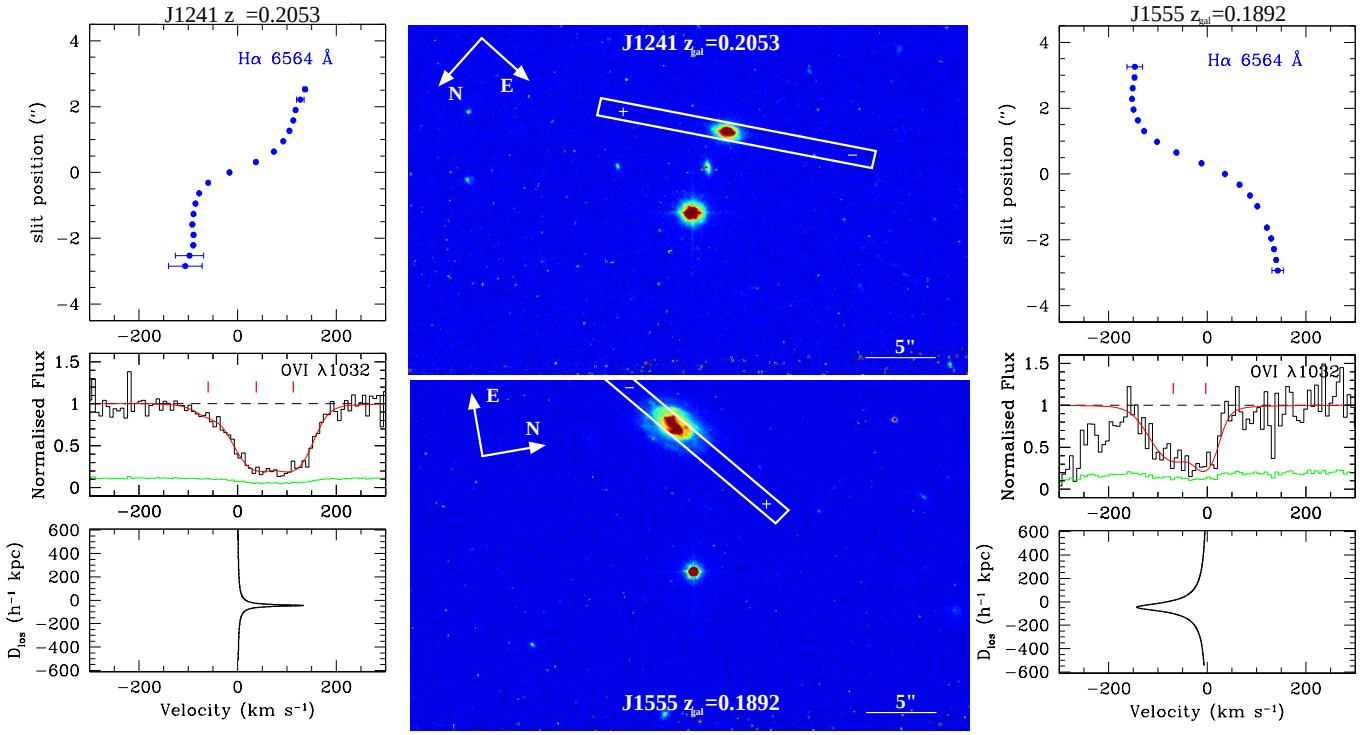

FIG. B4.— Same as Figure A1 except for top-middle and left is for the J1241 field with the $z = 0.2053$ galaxy and bottom-middle and right is for J1555 field with the $z = 0.1892$ galaxy. In both cases, the galaxies are co-rotating with respect to the O VI absorption.

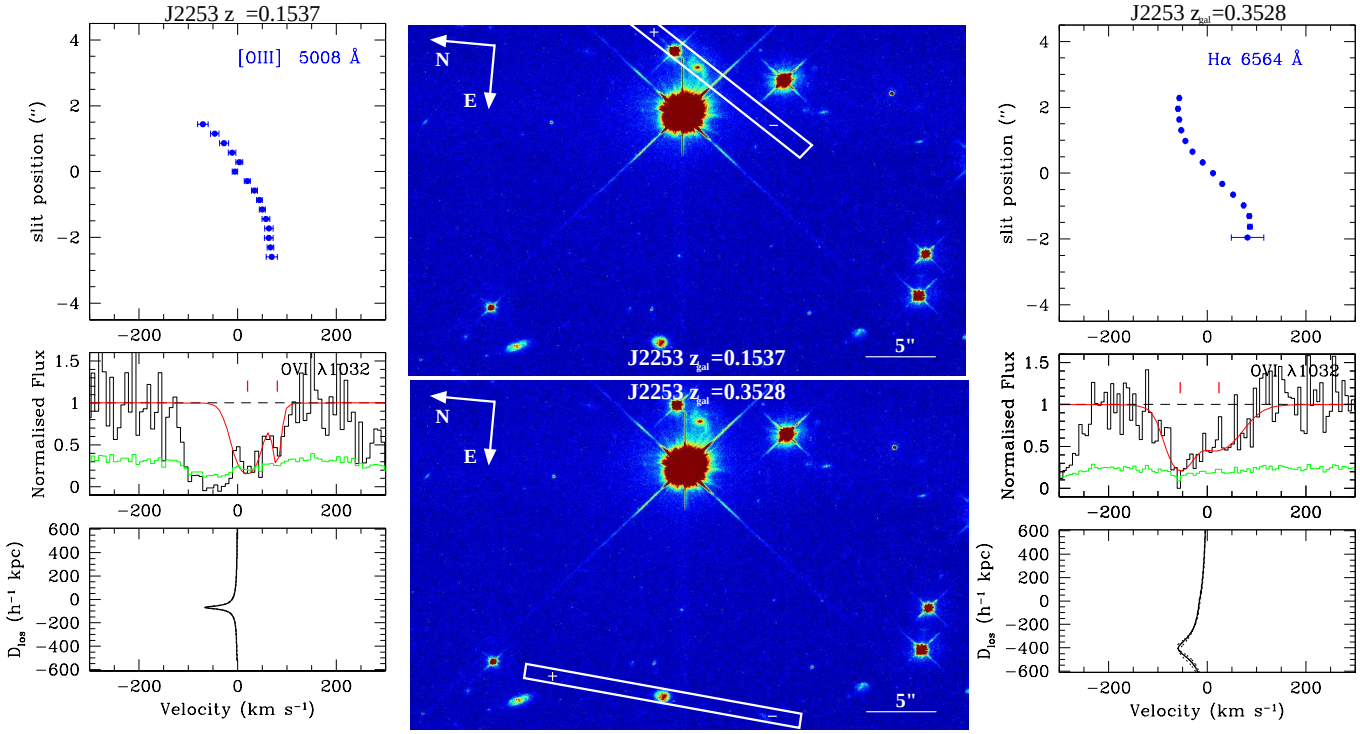

FIG. B5.— Same as Figure A1 except the middle top and bottom panels is for the J2253 field. The left panel is shown for the $z = 0.1537$ galaxy and the right is shown $z = 0.3528$ galaxy. The O VI for both galaxies spans boths sides of the systemic velocity, the galaxies are co-rotating with the highest optical depth O VI absorption.